Department of Physics and Astronomy
Heidelberg University

Bachelor Thesis in Physics

submitted by

Matthias Hans Heinrich Schmitt

born in Ulm (Germany)

2002

Investigation of low-frequency vibrational modes in representative thermotropic liquid crystals

This Bachelor Thesis has been carried out by Matthias Hans Heinrich Schmitt at the
Max-Planck-Institute for Nuclear Physics Institute in Heidelberg
under the supervision of
Dr. Laura Cattaneo

Year: 2024
Title: Investigation of low-frequency vibrational modes
          in representative thermotropic liquid crystals
Author: Matthias Hans Heinrich Schmitt

Acknowledgements

Abstract

0.1 English

This thesis is dedicated to a systematic study of the vibrational dynamics of representative thermotropic liquid crystals (LCs) in the spectral range from 1 to 7.5 THz. In particular, we measured the absorption spectra of two calamitic LCs, namely 4'-octyl-4-biphenylcarbonitrile (8CB), 4'-octyloxy-4-biphenylcarbonitrile (8OCB) and their mixtures, and two discotic LCs, hexabutoxytriphenylene (HAT4) and hexapentyloxytriphenylene (HAT5). These four molecules have been chosen to elucidate the role of specific atomic constituents and the molecular structure when inducing low-frequency vibrational modes. The first two are elongated and flexible, whereas the second is disk-like shaped and highly rigid, especially the core. We observed that 8OCB exhibited blue-shifting in low frequencies, spectral smoothing, and unclear differences at specific frequencies. Quantification of 8OCB's peak at $7\,THz$ awaits future experiments. Strong interactions between 8CB and 8OCB, especially at higher 8CB concentrations and field strengths, were inferred. The non-linear activity was minimal in pure 8CB but pronounced in a 75% 8OCB mixture, suggesting a non-linear interaction-based cause. The experimental cases have been compared with DFT calculations considering only single molecules, thus neglecting any inter-molecular dynamics. On the other hand, the discotic molecules exhibited stronger absorbance in their extraordinary axis than in their ordinary axis, thus indicating higher molecular stiffness, the longer HATn's alkoxy groups get.

0.2   Deutsch

Diese Arbeit ist einer systematischen Untersuchung der Schwingungs-
dynamik repräsentativer thermotroper Flüssigkristalle (LCs) im Spektral-
bereich von 1 bis 7,5 THz gewidmet. Insbesondere haben wir die Absorp-
tionsspektren von zwei kalamitischen LCs, nämlich 4'-Octyl-4-biphenyl-
carbonitril (8CB), 4'-Octyloxy-4-biphenylcarbonitril (8OCB) und deren Mis-
chungen, sowie von zwei diskotischen LCs, Hexabutoxytriphenylen (HAT4)
und Hexapentyloxytriphenylen (HAT5), gemessen. Diese vier Moleküle
wurden ausgewählt, um die Rolle spezifischer atomarer Bestandteile und
die Molekülstruktur duch Induktion niederfrequenter Schwingungsmoden
zu enthüllen. Die ersten beiden Moleküle sind langgestreckt und flexibel,
während das zweite Molekül scheibenförmig und sehr starr ist, insbesondere
der Kern. Wir beobachteten, dass 8OCB eine Blauverschiebung bei niedrigen
Frequenzen, eine spektrale Glättung und unklare Unterschiede bei bestim-
mten Frequenzen aufweist. Die Quantifizierung des lokalen Maximums der
Absorption von 8OCB bei $7\,THz$ steht noch aus. Es wurden starke Wech-
selwirkungen zwischen 8CB und 8OCB, insbesondere bei höheren 8CB-
Konzentrationen und Feldstärken, festgestellt. Die nichtlineare Aktivität war
bei reinem 8CB minimal, bei einer 75-prozentigen 8OCB-Mischung jedoch
ausgeprägt, was auf eine nichtlineare Wechselwirkung schließen lässt. Die
experimentellen Messungen wurden mit DFT-Berechnungen verglichen,
bei denen nur einzelne Moleküle berücksichtigt wurden, sodass jegliche
intermolekulare Dynamik vernachlässigt wurde. Andererseits zeigten die
diskotischen Moleküle eine stärkere Absorption in ihrer außergewöhnlichen
Achse als in ihrer gewöhnlichen Achse, was auf eine höhere molekulare
Steifheit hinweist, je länger die Alkoxygruppen von HATn werden.

Keywords: 8OCB/8CB interaction   -   non-linear response   -
liquid crystal   -   HAT4/HAT5

Contents

Chapter 1

Introduction

Liquid Crystals (LCs) exhibit different solid and liquid properties within the same mesophase. Since their discovery in 1888 [1], LCs gained ongoing interest from science and technology due to their outstanding properties in terms of birefringence, polarisability, and their response to external influences, e.g. electric and magnetic fields. Therefore, LCs became ideal candidates for opto-electronic technologies such as tunable wave plates, displays and "smart" glass in the visible to infrared wavelengths [2][3][4][5]. The wavelengths associated with THz radiation (0.1 - 10 THz) are long (3000 - 30 μ m). However, obtaining an appropriate phase shift requires a significantly larger thickness of the LC in the THz range in comparison with optical frequencies. Thus, losses are no longer negligible and form thereby the picture of an ideal LC; high birefringence and low losses at THz frequencies. Hence, systematic knowledge about various LCs in the THz range has to be acquired, which will result in a better understanding of how the ideal LC is structured. Consequently, a clear understanding of which molecular structure or composition causes which THz-response would help to synthesise new materials.

Chapter 2

Background

Liquid Crystal

Liquid crystals (LCs) are materials exhibiting one or several mesomorphic phases between their solid and liquid phase. Organic molecules performing those transitions as their temperature rises, are considered to be thermotropic **liquid crystals (LCs)** [6]. Moreover, there is a second class of LCs, lyotropic liquid crystals, changing its phases due to concentration changes, which we won't focus on in this work. Hence, we refer to thermotropic crystals when talking about LCs. These liquid crystalline phases between the crystalline solid and the liquid phase posses different mechanical, optical and structural properties. Such behaviour is exhibited by several different systems; e.g. certain classes of organic molecules, micellar solutions of surfactants, main and side chain polymers and a vast amount of biological systems are known to be liquid crystalline [7] [6]. Moreover, a liquid crystalline phase is, in a more general definition, an intermediate phase which possesses on the one hand a degree of order, and on the other hand, it has a liquid-like character in terms of free movement in at least one direction [8]. There are different types of ordering of anisotropic objects. Firstly, *orientational order* (OO) is given, if the symmetry axes of the ordering objects are on average parallel to a spacial direction, $\vec{n}$, known as *director*. To quantify the degree of OO, we introduce the order parameter:

$$S = \frac{1}{2} \left\langle 3\cos^2(\beta) - 1 \right\rangle, \qquad (2.1)$$

where β denotes the molecules angle respective to $\vec{n}$. The average over all molecules is expressed by the angled brackets. If $S = 1$, we can talk of perfect orientational order. Whereas, if $S = 0$, the molecules are isotropically distributed in orientation. Furthermore, we can define *positional order* (PO) as an invariance under translation by an integer times a lattice vector.

2.1 Calamitic LCs

Certain substances which exhibit liquid crystalline phases are formed of organic molecules with a length to diameter ratio of about 3-8 [6], which can be regarded as short rods. These LCs are named **calamitic** LCs, from the Latin word *calamus* which means reed. All molecules of this kind comprise a central rigid core connected to a flexible alkyl chain at one or both ends [6]. In the following, I want to introduce the two most common phases.

2.1.1 Nematic

The *nematic* phase differs just in its OO from an isotropic state. In other words, all molecules are on average aligned along a certain director, $\vec{n}$, while exhibiting liquid like properties; no positional order between the molecule centers (see Fig. 2.1). Typically, the order parameters S are about $0.3 - 0.5$ [3]. Moreover, many LC compounds possess a permanent dipole and thus are easily aligned by applying an external field [9]. The applica-

Figure 2.1: Nematic phase

tion of an external field has influence on the order parameter [10] and defines the crystal axes. Furthermore, nematic LCs can exhibit high birefringence ($\Delta n > 0.2$) [11]. Due to their birefringence, LC phases can be visually studied under a microscope with two crossed polarisers and a $\lambda/4$-plate, which is called polarised light microscopy. The eponymous thread structure can be observed with such a microscope, see Fig. 2.2a.
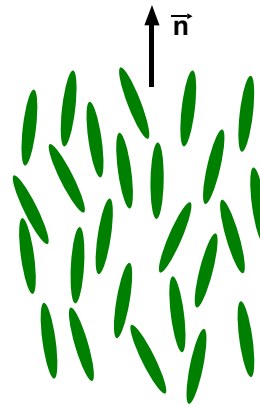
(a) Nematic   (b) Smectic A

Figure 2.2: Calamitic LC phases under a polarised light microscope (25% 8OCB, 75% 8CB). The nematic phase exhibits homogeneous structure, whereas smectic A shows its focal conic texture. The lines in (a) are caused by scraches and impurities of the cell windows' surfaces. The small particles, present in both phases, are impurities within the sample volume.

2.1.2 Smectic A

In contrast to the nematic phase, the molecules in a smectic phase are ordered in layers along one axis, which is for smectic A the director. Thus, the LC possesses *positional order* only in one dimension. Therefore, a LC in a *smectic* phase can be regarded as a two dimensional fluid [6]. Both smectic forms represent an aligned structure in respect to the director. Under a polarised light microscope, the smectic phases exhibit often a typical focal conic texture [9] (see Fig. 2.2b). The only difference between the *A* (SmA) and the *C* (SmC) form is the relative angle between the orientation of the LC molecules and the layer normal, which is $\neq 0°$ for smecic C (see Fig. 2.3). That should illustrate why the smectic A and nematic phase are referred to as *non-tilted* phases, whereas the smectic C phase is not.

(a) SmA   (b) SmC
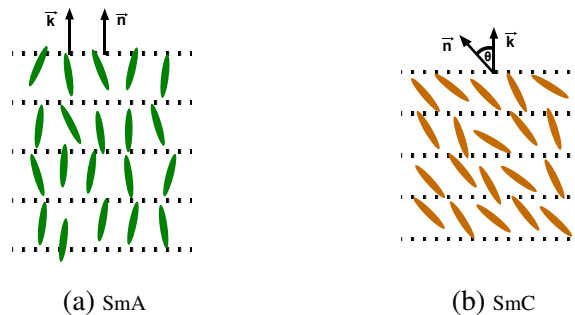
Figure 2.3: Calamitic LC phases: rod-shaped molecules oriented along $\vec{n}$ and located in separate layers.

2.1.3   8CB & 8OCB

8CB and 8OCB are two LCs which exhibit isotropic, nematic, smectic A and crystalline phases [13]. The transition temperatures can be found in Table 2.1. Note that the abbreviations $T_{Cr,SmA}$ corresponds to the crystalline–smectic A, $T_{SmA,N}$ represents the smectic A–nematic and $T_{N,I}$ is the short form of nematic–isotropic transition temperature.

Figure 2.4: Formular structure: (b) 8CB and (a) 8OCB [12].
The number before the "CB" (cyanobiphenyl) / "OCB" (octylbiphenyl) indicates the number of CH groups in the hydrocarbon tail.

The molecules are made out of an alkyl chain, two phenyl groups, a polar cyano group. 8OCB differs clearly by the presence of an extra oxygen atom between the biphenyl group and the alkyl chain (see Fig. 2.4). The permanent dipole allows to orient the molecules along their long axis ($\parallel \vec{n}$) and the other two perpendicular axes are symmetric, since the rotation of the individual molecules is generally not restricted in this plane. Consequently, the aligned crystal can be seen as an uniaxial crystal with $\vec{n}$ as the extraordinary axis and the perpendicular axes as oridnary axes. The chemical nomenclatures are 4'-octyl-4-biphenylcarbonitrile and 4'-octyloxy-4-biphenylcarbonitrile. Furthermore, mixtures of 8CB and 8OCB, in both 3 to 1 and 1 to 3 ratios, should show clear isotropic, nematic and smectic A phases too [14].

	$T_{Cr,SmA}$	$T_{SmA,N}$	$T_{N,I}$
8 CB	19.74°C	29.07°C	39.07°C
8 OCB	52.86°C	66.65°C	79.10°C

Table 2.1: Transition temperatures for pure 8CB and 8OCB received from [15] [16].

2.2   Discotic LCs

Disk-shaped molecules exhibiting liquid crystalline phases are commonly classified as discotic LCs. The nematic and columnar phases are the most common structural appearance of those LCs. Similar to the calamitic nematic phase, the discotic nematic phase (N_D) is merely defined by OO with the orientation along a characteristic axis of the molecule, which in this case is the short axis [6] (see Fig. 2.5b).

(a) Columnar phase   (b) N_D
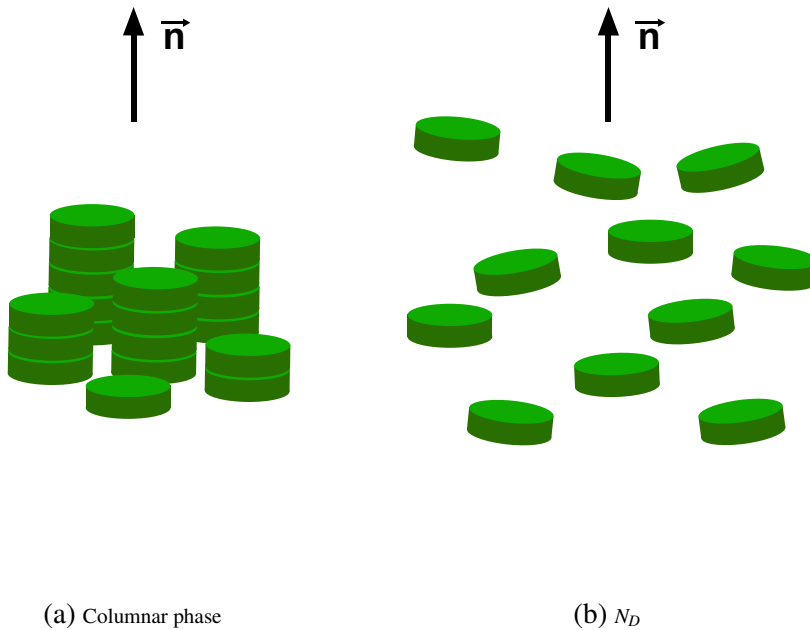
Figure 2.5: Discotic LC phases: A rising Temperature in the medium leads to a phase transition from (a) to (b).

The simplest columnar phase is represented by stacks of the corresponding disk-shaped molecules, forming a one-dimensional liquid-like structure. Consequently, the columns themselves form a rectangular or hexagonal two-dimensional lattice [6] (see Fig. 2.5a).

2.2.1 HATn

HATn is the abbreviation of the liquid crystal class Hexakis(n-alkoxy)triphenylene, with varying n. The n determines how long the alkoxy group is. We will only focus on n = 4,5. The discotic LC HAT5 exhibits in samples with a thickness of a few μm a crystalline, columnar and isotropic phase ($T_{CrCl} \approx 69°C$, $T_{ClI} \approx 122°C$)[17]. The transition temperatures are higher for HAT4, which has the shorter alkoxy groups ($T_{CrCl} \approx 88°C$, $T_{ClI} \approx 144°C$)[18]. Moreover, the LC HAT4 has shown

Figure 2.6: HAT5 structure [17]

enhanced electron mobility when inserted to an organic solar cell [19]. It isn't possible to align the HATn LCs by an external field since the molecules do not have strongly polar groups and are on top of that very symmetric (see Fig. 2.6).

2.3 THz radiation

As mentioned in the introduction, the oscillation period associated with THz radiation ($0.1 - 10 THz$) are long ($100 fs - 10 ps$) compared to the visible spectrum. Consequently, THz radiation reveals dynamics in materials such as lattice vibration [20], spin precession periods [21] [22] and electron momentum scattering [23], since those processes take mostly place on a time scale within the THz range [24].

For table top set-ups, THz radiation is commonly generated by non-linear optics and not by a convenient THz laser. This is due to the fact that a direct state transition with an energy difference of $1 THz$ is only efficient at extremely low temperatures, if you assume a simple two-level thermal population system and apply Maxwell-Boltzmann statistics. Furthermore, blackbody emission allows, according to Planck's law, merely a very weak radiance[1] in the particular frequency range and more importantly the radiation won't be coherent. Note, there exist large facilities that use relativistic free electrons to create THz generation, e.g. free-electron laser (FEL) [25]. However, different non-linear sources have stood out and proven successful

---

[1]calculated with Planck's law

in generating THz radiation, e.g. optical rectification in inorganic crystals (e.g. GaP [26]) and organic crystals (e.g. DSTMS [26]). In the following, I want to focus on this kind of non-linear THz generation, since it is the technique which has been used in the experiments which are discussed later.

2.3.1 Non-linear optics for THz generation

We conventionally write the polarisation density P in a general medium as a sum of linear and non-linear (P^{NL}) parts [27]

$$P_i(t) = \varepsilon_0 \sum_j \chi_{ij} E_j(t) + P_i^{NL}, \tag{2.2}$$

where E represents the external electrical Field, ε_0 the permittivity of free space and χ the electric susceptibility for a linear dielectric. P^{NL} represents an expansion of all non-linear combinations of the electric field and hence can be described by its tensorial nature

$$P_i^{NL} = \sum_{j,k} \varepsilon_0 \chi_{ijk}^{(2)} E_j(t) E_k(t) + \sum_{j,k,l} \varepsilon_0 \chi_{ijkl}^{(3)} E_j(t) E_k(t) E_l(t) + ..., \tag{2.3}$$

where the coefficients of the n-th order terms are summarized in the $(n+1)$-rank tensor $\chi_{...}^{(n)}$. Compared to the linear case, the second temporal derivative of the polarisation presents additional terms, which are summarized by the source S, when considering the wave equation for a non-linear medium [28]

$$\nabla^2 E - \frac{n^2}{c_o^2} \frac{\partial^2 E}{\partial t^2} = -S, \tag{2.4}$$

$$S = -\mu_0 \frac{\partial^2 P_{NL}}{\partial t^2}. \tag{2.5}$$

The term S is usually regarded as a source that radiates in a linear medium with refractive index n and is dependent on the second temporal derivative of the non-linear polarisation density. Evidently, this formulation of non-linearity is general. Thus, the first approach is to limit the non-linearity to a certain degree and to focus on the main contributions. The experiment set-up includes material which exhibits a high second order contribution in its polarisability. Hence, a more detailed explanation is necessary.

Second-Harmonic Generation (SHG) & Optical Rectification (OR)

For defining and explaining these two phenomena in non-linear optics, we will first build up a model with formalism.

For modelling the non-linear response of a medium, we use the Lorentz model which is a damped externally driven oscillator with an additional non-linear term [29]

$$\frac{d^2x}{dt^2} + \gamma\frac{dx}{dt} + \omega_0^2 x + \alpha x^2 = -\frac{e}{m}E(t)\,. \tag{2.6}$$

This choice is appropriate, since the incident radiation represents a driving force $(-eE)$, and the harmonic oscillator equation (terms linear in x) is expanded by a non-linear term (αx^2) which is the simplest version of modulating the potential energy to an asymmetric potential energy. The idea of an asymmetric potential energy is adequate for non-linear optical interaction encountering a non-symmetric charge distribution within the medium.

Now we assume a harmonic incident electric field, e.g. $E(t) = E_0 \cdot e^{-iwt}$. Furthermore, it is valid to expand $x(t) = \sum_{n=1}^{\infty} x^{(n)}(t)$ in the perturbative regime where $\alpha x^2 < \omega_0^2 x$. Note that $x^{(n)} \propto (E_0)^{(n)}$. Plugging this sum into Eq. (2.6) yields a set of linked differential equations. Since we neglect higher terms than second order, only two equations are left:

$$\frac{d^2x^{(1)}}{dt^2} + \gamma\frac{dx^{(1)}}{dt} + \omega_0^2 x^{(1)} = -\frac{e}{m}E(t)\,, \tag{2.7}$$

$$\frac{d^2x^{(2)}}{dt^2} + \gamma\frac{dx^{(2)}}{dt} + \omega_0^2 x^{(2)} = -\alpha\left[x^{(1)}\right]^2\,. \tag{2.8}$$

The first Eq. (2.7) is a driven, damped oscillator and its well-known solution reveals, by substituting into Eq. (2.8), the second-order response:

$$x^{(2)}(t) = x_{2\omega}^{(2)} + x_0^{(2)}\,, \tag{2.9}$$

$$= -\alpha\left[\frac{eE_0}{m}\right]^2 \frac{e^{-i2\omega t}}{(\omega_0^2 - \omega^2 - i\omega\gamma)^2(\omega_0^2 - (2\omega)^2 - i2\omega\gamma)} + \text{c.c.}$$

$$- 2\alpha\left[\frac{e}{m\omega_0}\right]^2 \frac{|E_0|^2}{(\omega_0^2 - \omega^2)^2 + \omega^2\gamma^2}\,, \tag{2.10}$$

where the two time-dependent terms represent the charge oscillation in a non-harmonic potential ($U = \frac{1}{2}\omega_0^2 x^2 + \frac{1}{3}\alpha x^3$) [30] occurring and radiating at twice the incoming frequency. Due to this radiation at 2ω, it is referred to as *second-harmonic generation (SHG)*. Whereas, the last and time independent term Eq. (2.10) describes the average charge displacement under induced oscillation in the chosen non-harmonic potential; representing a non-radiating DC field for incident continuous wave (CW) radiation; and is often classified as *optical rectification (OR)*. The polarisation created by this optical rectification is

$$P^{(2)}(0) = -Nex_0^{(2)} = \frac{2\alpha e^2 N}{m^2\omega_0^2((\omega_0^2 - \omega^2)^2 + \omega^2\gamma^2)}|E_0|^2 \equiv 2\varepsilon_0\chi^{(2)}(0,\omega,-\omega)|E_0|^2.$$

(2.11)

Here we defined the second-order non-linear optical susceptibility $\chi^{(2)}(0,\omega,-\omega)$ corresponding to the optical rectification process. Consequently, the most general form of the optical rectification, since non-uniform media exist, induced polarisation is obtained as [29]

$$P_i^{(2)}(0) = \sum_{j,k}\varepsilon_0\chi_{ijk}^{(2)}(0,\omega,-\omega)E_j(\omega)\overline{E_k}(\omega).$$

(2.12)

A corresponding polarisation for SHG can be defined in the same manner as in Eq. (2.11).

So far we have only considered incident CWs, however it is necessary to study pulsed signals when working with pulsed lasers. As we can notice in the OR term Eq. (2.10), the displacement and hence the polarisation are only dependent on the amplitude of the signal, regardless the frequency. Consequently, the OR polarisation will be influenced by the envelope of the pulsed signal, and a time dependency, and thus radiate according to Eq. (2.5). Note that $P^{(2)}(0)$ does not radiate for a CW, but for a pulsed wave (see Fig. 2.7).

The crystal 4-N,N-dimethylamino-4'-N'-methyl-stilbazolium 2,4,6-tri-methylbenzenesulfonate (DSTMS), which is used in our setup, has a high conversion efficiency regarding OR ($\eta(DSTMS) \sim 2 \cdot 10^{-4}$ [26]) compared to GaP ($\eta(GaP) \sim 2 \cdot 10^{-5}$ [26]) and is well phase matched for OR [31].

(a) Incident continuous wave (CW)   (b) Pulsed incident wave
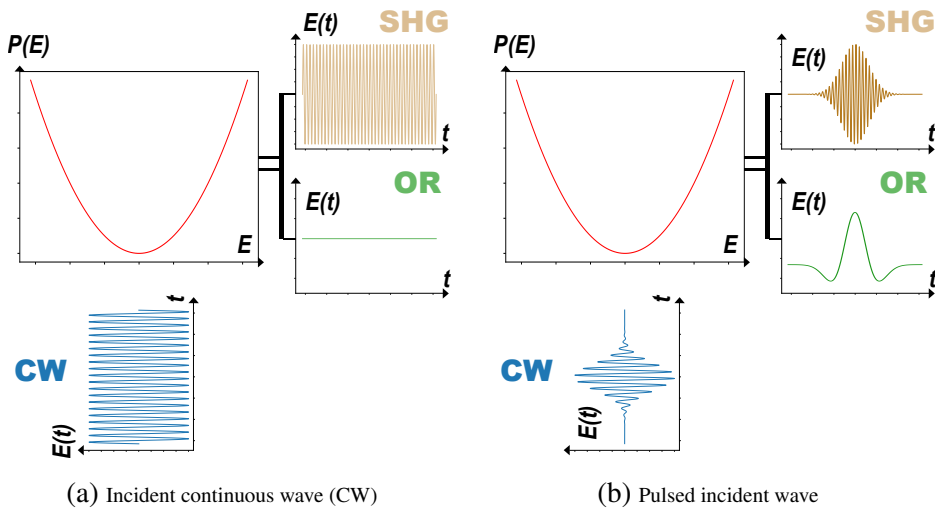
Figure 2.7: SHG and OR visualisation:
An incoming wave (CW or pulsed wave) changes the polarisation (red) of the medium. The radiated second temporal derivatives of the polarisation are sketched on the right of each figure (SHG and OR).

2.3.2 THz detection

In the past decades, several THz detection techniques have been tested and developed. Notably, photoconductive antennas and electro-optical sampling are the most common techniques [32]. The subsequent elaboration will exclusively focus on electro-optical sampling. The underlying process, the Pockels-effect, will be studied along the example of a GaP crystal.

Pockels-effect

The refractive index ellipsoid for a uniaxial crystal is given in the standard crystallographic coordinate system (X, Y, Z) in the absence of an electric field by [33]

$$\frac{X^2}{n_o^2} + \frac{Y^2}{n_o^2} + \frac{Z^2}{n_o^2} = 1 \,. \tag{2.13}$$

For GaP, a crystal of point group $\bar{4}3m$, the equation changes under the influence of an electric field in the following manner [33]:

$$\frac{X^2}{n_o^2} + \frac{Y^2}{n_o^2} + \frac{Z^2}{n_o^2} + 2r_{41}E_X YZ + 2r_{41}E_Y XZ + 2r_{41}E_Z XY = 1. \qquad (2.14)$$

In the following, the influence on the refraction properties of a GaP crystal, rather its $[110]$ cut as illustrated in Fig. 2.8, is elaborated. For our purposes, we consider only an incident electric field propagating normal to this plane and for simplicity $E \parallel \begin{pmatrix} -1 & 1 & 0 \end{pmatrix}^T$. A first approach is replacing the coordinates (X,Y,Z) (see Fig. 2.8, black axes) in Eq. (2.14) by the crystal system coordinates (x,y,z) (see Fig. 2.8, blue axes)
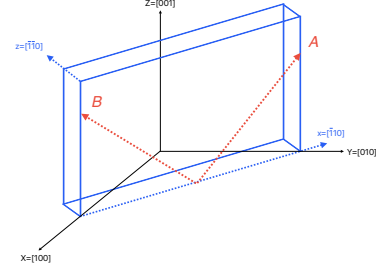
Figure 2.8: Coordinate system with a crystal cut of the (110)-plane

$$x = \frac{1}{\sqrt{2}} \begin{pmatrix} -1 \\ 1 \\ 0 \end{pmatrix}, \qquad y = \begin{pmatrix} 0 \\ 0 \\ 1 \end{pmatrix}, \qquad z = \frac{1}{\sqrt{2}} \begin{pmatrix} -1 \\ -1 \\ 0 \end{pmatrix}, \qquad (2.15)$$

$$\begin{pmatrix} 1 \\ 0 \\ 0 \end{pmatrix} = X = -\frac{x+z}{\sqrt{2}}, \qquad \begin{pmatrix} 0 \\ 1 \\ 0 \end{pmatrix} = Y = \frac{x-z}{\sqrt{2}}, \qquad \begin{pmatrix} 0 \\ 0 \\ 1 \end{pmatrix} = Z = y, \qquad (2.16)$$

and replacing the electric field, how we assume it, in the following way:

$$E = E_{THz} \begin{pmatrix} 1 \\ 0 \\ 0 \end{pmatrix}_{(x,y,z)} = \frac{E_{THz}}{\sqrt{2}} \begin{pmatrix} -1 \\ 1 \\ 0 \end{pmatrix}_{(X,Y,Z)} \qquad \Rightarrow \qquad E_X = \frac{-E_x}{\sqrt{2}} = -E_Y. \qquad (2.17)$$

This yields to the form of the refractive index ellipsoid

$$\frac{x^2}{n_o^2} + \frac{z^2}{n_o^2} + \frac{y^2}{n_o^2} - 2r_{41}E_x xy = 1. \qquad (2.18)$$

Unfortunately, this chosen coordinate system is not the new principal-axis coordinate system. However, we can clearly see how to change our

choice to make things work. Therefore, we have to define two new axes *A* and *B* (see Fig. 2.8, red axes):

$$A = \frac{x+y}{\sqrt{2}}, \qquad\qquad B = \frac{y-x}{\sqrt{2}}, \qquad\qquad (2.19)$$

and accordingly change the axes again:

$$\frac{z^2}{n_o^2} + \frac{A^2}{n_o^2} + \frac{B^2}{n_o^2} + r_{41}E_x(B^2 - A^2) = 1. \qquad\qquad (2.20)$$

To obtain the implicitly defined refractive indices along *A* and *B*, we just have to satisfy

$$\frac{B^2}{n_B^2} + \frac{A^2}{n_A^2} + \frac{z^2}{n_o^2} = 1. \qquad\qquad (2.21)$$

In the physical realistic limit $r_{41}E_x << \frac{1}{n_0^2}$, the refractive indices behave like [30]

$$n_A = n_o + \frac{1}{2}n_o^3 r_{41}E_x. \qquad\qquad (2.22)$$

$$n_B = n_o - \frac{1}{2}n_o^3 r_{41}E_x. \qquad\qquad (2.23)$$

and the difference of the two refractive indices, $\Delta n = n_0^3 \cdot r_{41} \cdot E$, is referred to as the Pockels-effect. This creation of birefringence by an external stimulus is the core element of electro-optical sampling.

Electro-optical sampling

The core principle of electro-optical sampling is the Pockels-effect. The external field is provided by the THz beam, whereas the probe beam will experience the different refractive indices. The pulse length of the probe beam is chosen significantly shorter than the THz beam's pulse length. Thus, the THz field can be regarded as constant in the time window of the probe beam pulse. As described in section 2.3.2, a different polarisation of the crystal causes field dependent refractive index changes. The probe

will experience two different refractive indices and consequently leave the crystal elliptically polarised. Furthermore, the phase difference between those two axis can be determined by using section 2.3.2:

$$\Delta\phi = (n_A - n_B)\frac{\omega d}{c} = \frac{\omega d}{c}n_o^3 r_{41}E_{THz}, \qquad (2.24)$$

with d being the thickness of the crystal along the probe's propagation. The more intense the polarisation of the crystal, the higher the eccentricity. Moreover, the phase shift is proportional to the THz field strength. Considering no THz field, the probe's electric field would just linearly propagate through the crystal. A subsequent $\lambda/4$ plate ,whose axis are rotated by $45°$ relative to the probe's polarisation, turns the linear polarisation into circular polarisation (see Fig. 2.9).

(a) $E_{THz} = 0$ (b) $E_{THz} \neq 0$
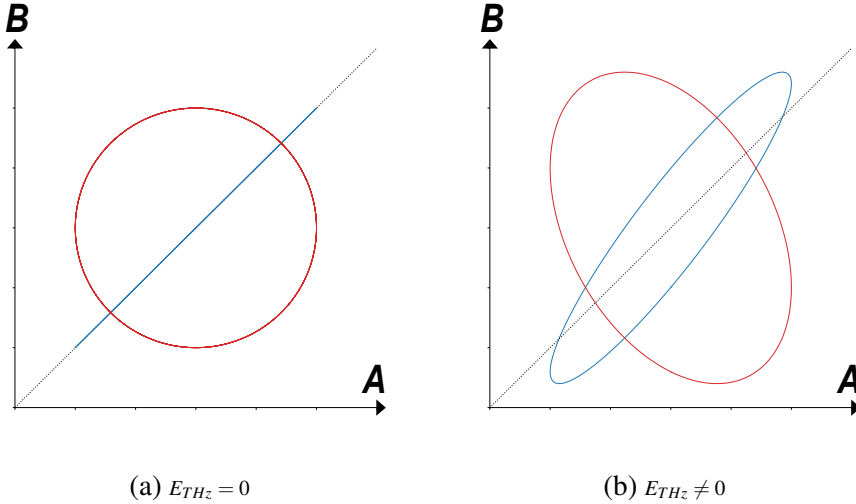
Figure 2.9: Examplar polarisation of the probe beam after passing the GaP crystal (blue) and $\lambda/4$-plate (red). We assumed for (b) $n_B < n_A$ and $\Delta\phi = \pi/8$.

In presence of a non-zero THz field, the previously linearly polarised probe beam leaves the GaP crystal elliptically polarised. The $\lambda/4$ -plate changes the eccentricity and the phase between the components along A and B (for more details see Appendix).

A subsequent Wollaston prism splits the horizontal and vertical components of the elliptically polarised light in two separate beams under a specific angle. Those beams are guided onto two separate detectors and consequently the intensity difference can be evaluated. The intensities of the two probe

beams at the photo diodes are [29]

$$I_B = \frac{I_0}{2}(1 - \sin\Delta\phi) \approx \frac{I_0}{2}(1 - \Delta\phi), \tag{2.25}$$

$$I_A = \frac{I_0}{2}(1 + \sin\Delta\phi) \approx \frac{I_0}{2}(1 + \Delta\phi), \tag{2.26}$$

where I_0 is the initial intensity of the probe. As long as the external field is zero, this distribution of horizontal and vertical component should be equal and therefore the voltage difference between the two photo detectors should be in the order of the noise. For the general case, the difference of the photo diodes results in

$$\Delta I = I_A - I_B = I_0\Delta\phi = \frac{I_0\omega d}{c}n_o^3 r_{41}E_{THz}. \tag{2.27}$$

Rearranging the equation shows how E_{THz} is determined

$$E_{THz} = \frac{\Delta I}{I_0}\frac{c}{\omega d n_0^3 r}. \tag{2.28}$$
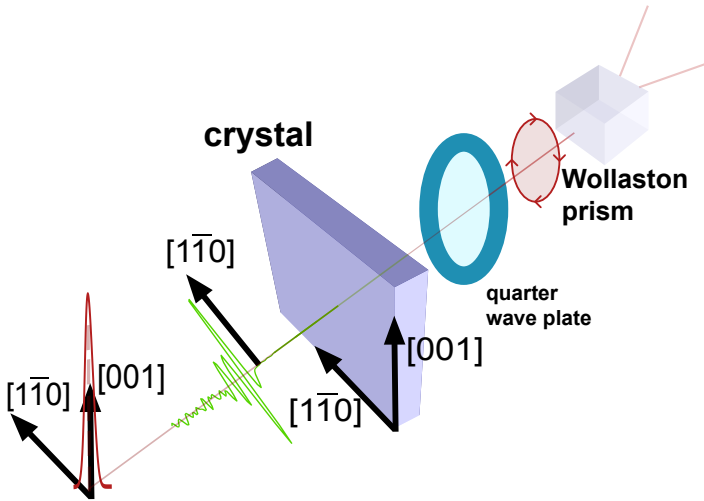
Figure 2.10: Electro-optical sampling
The probe beam (red) experiences, depending on the time delay relative to the THz beam (green), different birefringence in the crystal with (110) cut. The elliptically polarised light leaving the crystal has the same axes as the $\lambda/4$-plate and receives a phase shift of $\pi/2$ before being split in both components in the Wollaston prism.

2.4 THz time-domain spectroscopy

The name 'time domain spectroscopy' (TDS) is originating from the fact that the THz wave lengths are long enough to be mechanically scanned in the time domain by short optical pulses. The path length of the probe can be elongated or shortened and allows applying electro-optical sampling allong the entire THz pulse. In contrast to grating based spectroscopy, the frequency or absorption spectra of the scan data are retrieved by a fast Fourier transformation (FFT) of the incoming signal, which also has the advantage of retrieving the phase. Note, the measurements are relative and always compare the interaction of a reference volume with a previously, optically unknown sample volume. For implementing the measured signals properly, understanding the underlying physics, and drawing the right conclusions, the optical interaction with a sample must be elaborated.

2.4.1 Refractive index and absorbance of the sample

Let's begin with a propagating electromagnetic wave that can be written, at a time (e.g. $t = 0$), as

$$E(\omega, r) = A_E \cdot \exp(ikr) = A_E \cdot \exp(i\omega \frac{n(\omega)}{c} r), \qquad (2.29)$$

with k as wave number, r as coordinate of space and A_E the complex amplitude. Since we consider media different from air, the refractive index is in general complex,

$$\underline{n} = n + i\kappa, \qquad (2.30)$$

and we might extract its attenuating and phase shifting partitions. For doing so, we substitute Eq. (2.30) in Eq. (2.29):

$$E(\omega, r) = A_E \cdot \exp(i\omega \frac{n + i\kappa}{c} r) = A_E \cdot \exp(-\omega \frac{\kappa}{c} r) \exp(i\omega \frac{n}{c} r), \quad (2.31)$$

$$\equiv A_E \cdot \exp(\frac{-\alpha r}{2}) \exp(i\Delta\varphi_r r). \qquad (2.32)$$

Thus, we receive the absorption coefficient α, which describes the attenuation, and the phase shift $\Delta\varphi_r$.

For all our measurements, the LCs are confined in a cell. Consequently, we observe an electromagnetic wave entering 4 times different media, once

from nitrogen gas, $(n_{N_2} \approx 1)$ into the cell window, and from the cell window into the sample, and vice versa (see Fig. 2.11).
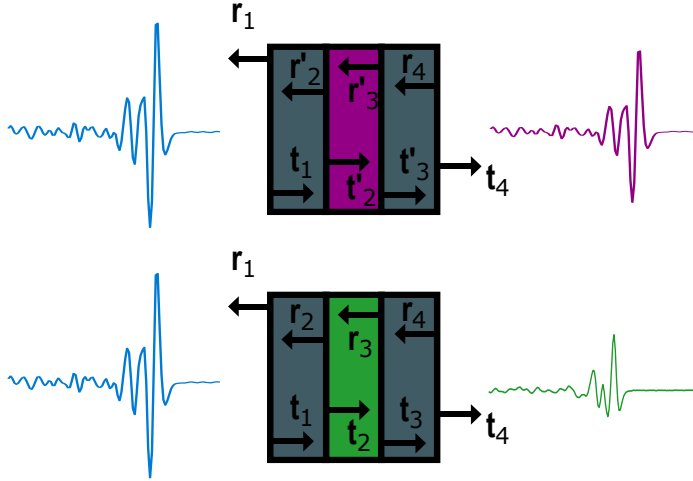
Figure 2.11: THz propagation through a cell
Top (reference cell): The initial THz beam (blue) propagates through the cell windows (grey) and the enclosed air (*violet*, $n \approx 1$), losing intensity.
Bottom (sample cell): The initial THz beam (blue) propagates through the cell windows (grey) and the enclosed sample volume (*green*), losing intensity and being modulated.

According to the Fresnel equations, the transmission coefficient for incident waves normal to the sample surface is

$$t = \frac{2n_i}{n_i + n_t},\tag{2.33}$$

with n_i for the refractive index of the medium where the incident wave is originating and n_t for the medium in which the wave is transmitted [28]. The refractive index of the cell windows will be noted as n_{win} and for the sample, when considering the cell to be filled with LC, we write n_{sam}. Note that the green volume in Fig. 2.11 is filled with air for a reference cell and consequently we can assume in this case $n \approx 1$. Considering all that, the remained first order wave, which continues propagating towards the detector, will be attenuated and its remaining fraction is:

$$t_{ref} = t_1 \cdot t_2 \cdot t_3 \cdot t_4 = \frac{2}{1 + n_{win}} \cdot \frac{2n_{win}}{n_{win} + 1} \cdot \frac{2}{1 + n_{win}} \cdot \frac{2n_{win}}{n_{win} + 1},\tag{2.34}$$

$$t_{sam} = t_1 \cdot t_2' \cdot t_3' \cdot t_4 = \frac{2}{1 + n_{win}} \cdot \frac{2n_{win}}{n_{win} + n_{sam}} \cdot \frac{2n_{sam}}{n_{sam} + n_{win}} \cdot \frac{2n_{win}}{n_{win} + 1}, \quad (2.35)$$

with t_{ref} considering only a cell filled with air, whereas t_{sam} represents the remainder of a sample filled with a certain LC. We prepared LC cells using COC polymers which exhibit a refractive index in the frequency range of the spectrometer of about $n_{COC} = 1.546 \pm 0.005$, which has been previously studied within the ULCD group. SiC, which is the second type of windows that has been used for this work, exhibits a slightly increasing refractive index from $n_{SiC} \approx 3.12$ at $2\,THz$ to $n_{SiC} \approx 3.18$ at $8.1\,THz$ [34]. For our data evaluation, we assume $n_{SiC} \approx 3.15 \pm 0.05$.

After considering the losses due to the reflections at the surfaces, the comparison of the the electric field of the reference E_{ref} and the electric field passing through the sample E_{sam} can be appropriately carried out by Eq. (2.29) and Eq. (2.32) :

$$E_{ref}(\omega, d) = t_{ref} \cdot A_E \cdot \exp(i\omega \frac{1}{c} d) \equiv A_{ref} \cdot \exp(i\phi_{ref}), \quad (2.36)$$

$$E_{sam}(\omega, d) = t_{sam} \cdot A_E \cdot \exp(\frac{-\alpha d}{2}) \exp(i\omega \frac{n}{c} d) \equiv A_{sam} \cdot \exp(i\phi_{sam}), \quad (2.37)$$

whereby the 0 of the r-axis is chosen as the surface facing the incoming beam. Considering the definition of the expressed phases $\phi_{ref} = \frac{\omega d}{c}$ and $\phi_{sam} = n\frac{\omega d}{c}$, the refractive index simply results as:

$$n(f) = \frac{\phi_{sam}(f) - \phi_{ref}(f)}{\frac{2\pi f}{c} d} + 1. \quad (2.38)$$

Consequently, the absorption coefficient can be evaluated by dividing Eq. (2.37) by Eq. (2.36) after taking the absolute value:

$$\frac{t_{sam}}{t_{ref}} \cdot \exp(\frac{-\alpha d}{2}) = \frac{|A_{sam}(f)|}{|A_{ref}|}, \quad (2.39)$$

$$\Rightarrow \alpha(f) = -\frac{2}{d} \cdot \ln\left(\frac{|A_{sam}(f)|}{|A_{ref}(f)|} \cdot \frac{(n_{sam} + n_{win})^2}{n_{sam} \cdot (1 + n_{win})^2} \right). \quad (2.40)$$

Gaussian error propagation allows us to estimate the absorbance's uncertainty with the cell thickness uncertainty Δd, as:

$$\Delta\alpha = \sqrt{\left(\frac{\Delta d}{d}\alpha\right)^2 + \frac{4}{d^2}\cdot\left(\left(\frac{\Delta|A_{sam}(f)|}{|A_{sam}(f)|}\right)^2 + \left(\frac{\Delta|A_{ref}(f)|}{|A_{ref}(f)|}\right)^2\right)}, \quad (2.41)$$

by neglecting the uncertainties in the refractive index for the sample and the windows in the frequency range which we are studying.

Chapter 3

Methods

3.1 Setup

3.1.1 Beam preparation

For enabling THz spectroscopy, a beam which is driving a non-linear process for THz generation is required, commonly called *pump* beam. In our case, the THz beam is created by OR with 1500*nm* pulses in a DSTMS crystal. This wave length has been chosen due to its good phase matching properties [31]. However, the lab possesses a pulsed 800*nm* laser; with a pulse energy of $9\mu J$; and we therefore use an optical parametric amp-

Figure 3.1: Preparation of probe (800nm) and pump (1500nm) beam

lifier (OPA) to generate a signal of 1500*nm* pulses. Nevertheless, to perform electro-optical sampling a *probe beam* is needed. This is realised by a beam splitter, which can be seen in figure Fig. 3.1. One part of the 800*nm* pulses continues propagating, whereas the other fraction runs through the OPA. The additional path length, caused by the processes in the OPA (ca. 3*m*), must be compensated, since the pulses should arrive exactly at the same time in the GaP crystal to obtain not only the spatial but also the temporal

overlap.

3.1.2   Spectrometer setup

The pulsed 1500*nm* beam reaches the first crystal, DSTMS, and creates
by OR THz radiation [26]. THz radiation is strongly absorbed by water
vapor [35] and therefore the relative humidity is held $< 3\%$ during the
measurements by purging its propagation volume with nitrogen gas N_2. The
residual IR, after the interaction with the DSTMS, is filtered out and the
THz beam is guided by parabolic mirrors to its second focal point, where it
interacts with the sample (see Fig. 3.2).
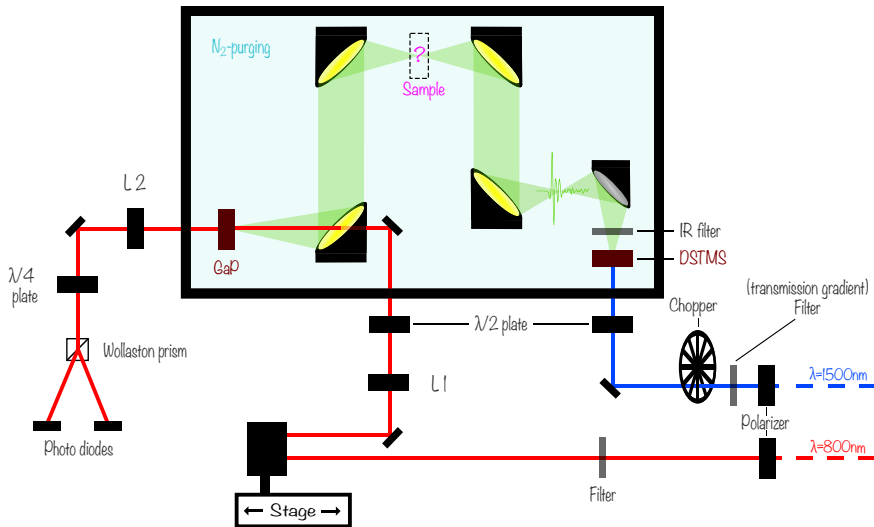
Figure 3.2: THz TD Spectrometer
The probe beams (red) path length can be modulated by a movable stage. The pump beam
(blue) is blocked and unblocked by a rotating chopper wheel ($500Hz$), which allows two
consecutive measurements reducing the noise.

Afterwards, the beam propagates in the same manner with the help of
parabolic mirrors into its last focal point, where the GaP crystal is placed.
We want to measure the complete THz signal and consequently we need a
time delay relative to the probe beam. This is realised by a movable stage
which modulates the path length of the probe beam (see Fig. 3.2). The probe
beam's pulse length (normally: $T \approx 35$fs) limits the spectral solution.

The advantage of using DSTMS over GaP for the THz generation lies
in the broader spectral range and the higher peak field that can be obtained
[26].

3.1.3 The Data acquisition

So far, the physical basis and the set-up have been explained. In the following, the data in Fig. 3.3 is used to illustrate the general data acquisition in the THz TD spectrometer. The received Voltage difference of the two photo diodes is measured and amplified ($\times 10$), while the remote-controlled mirror moves on the stage and consequently changes the path length of the probe beam. Each measurement is the average of at least 5 stage scans. The time domain (TD) pulse (Fig. 3.3a) is obtained from the positional stage data by taking the speed of light into account. Within this TD pulse, we receive a time delayed and attenuated second THz signal due to double reflection in the GaP crystal. Therefore, we are not interested in taking those parts into account, when calculating the frequency spectrum. Two Gaussian error functions are used to separate the useful signal from the rest (see Fig. 3.3a).

(a) Time domain pulse

(b) Frequency domain pulse

(c) Refractive index

(d) Absorbance
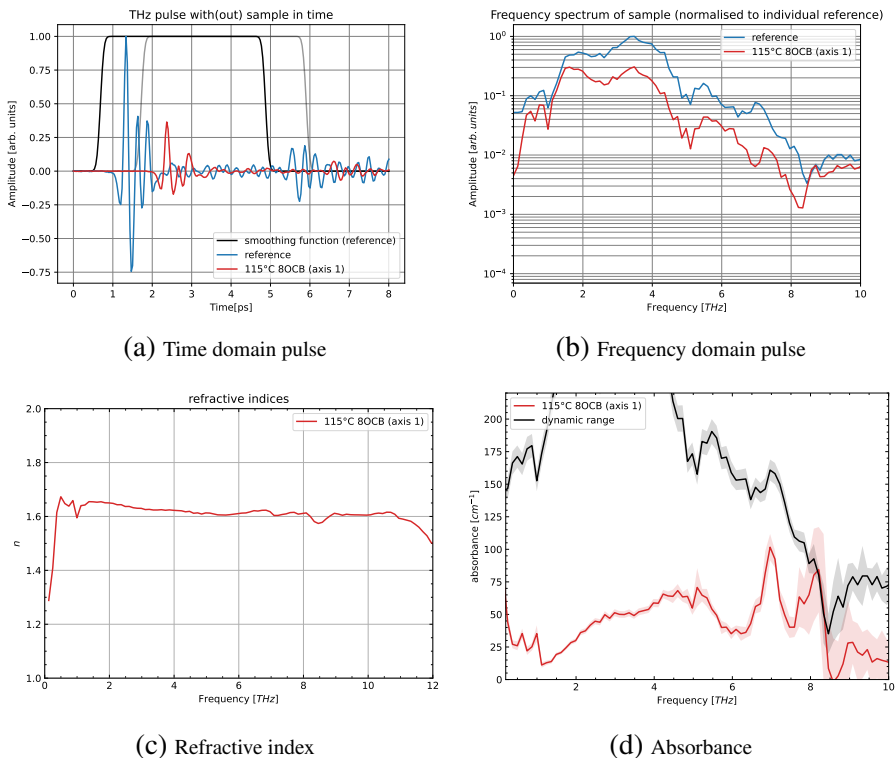
Figure 3.3: Exemplar data acquisition from the THz signal.
The grey curve in (a) is the smoothing function for the sample signal and therefore shifted by the retardation.

Furthermore, fast Fourier transform (FFT) is used to accomplish numer-

ical Fourier transformation of the TD signal, such that the absolute value represents the frequency in Fig. 3.3b. All measurements are normalised to the maximum of the reference spectrum, allowing good visualisation. Each stage scan is individually Fourier transformed (FT) and the average of all stage scans is calculated in the frequency domain (FD). The variance is obtained by statistical calculations in the FD data set and its average. Moreover, the complex phase of the FFT signal gives an insight into the phase propagation and enables the calculation of the refractive index Eq. (2.38). However, retrieving the actual propagating phase requires corrections, since the angle retrieval function has the bare domain of $(-\pi, \pi]$ [36]. Using the corrected refractive index and the frequency spectrum, the absorbance of the sample can be deduced with the formula Eq. (2.40). The absorbance's corresponding standard deviation is calculated as in Eq. (2.41).

We have to disregard our data above $8\,THz$, since our measurements reach the noise floor just below this frequency for most of the measurements. This means that we do not generate any significant THz fields above the $8\,THz$ and consequently cannot make meaningful statements about the absorbance. When discussing an absorbance spectrum, it is important to know that the data is within the *dynamic range*. By dynamic range we mean the maximal absorbance of the reference compared to the noise floor. In other words, we cannot measure a stronger absorbance than the dynamic range. The corresponding dynamic range for the exemplar signal is inserted in Fig. 3.3d. In general, the dynamic range can show if the actual amplitude of a particular frequency range may be underestimated.

3.1.4 Field strength determination

The previously discussed data acquisition can be done without knowing the actual field strength of the THz beam, since it is a relative measurement. However, we want to know the field strength, when studying non-linear responses of the samples. In order to do this, we place the GaP crystal in the position of the sample and guide the probe beam on a different path into the second focal point. The probe beam travels through the center of the two neighbouring parabolic mirrors and is propagating straight to the detector. We measure the diode intensities for different pulse intensities and calculate the THz field strength (Eq. (2.28)). The pulse intensity can be regulated by moving a intensity filter before the DSTMS (see Fig. 3.2).

Analysing the probe pulse intensity or energy versus the THz field strength reveals the saturation of the GaP for too high pulse energies (see Fig. 3.4). Consequently, additional attenuation is necessary before entering the eletro-optical sampling crystal.
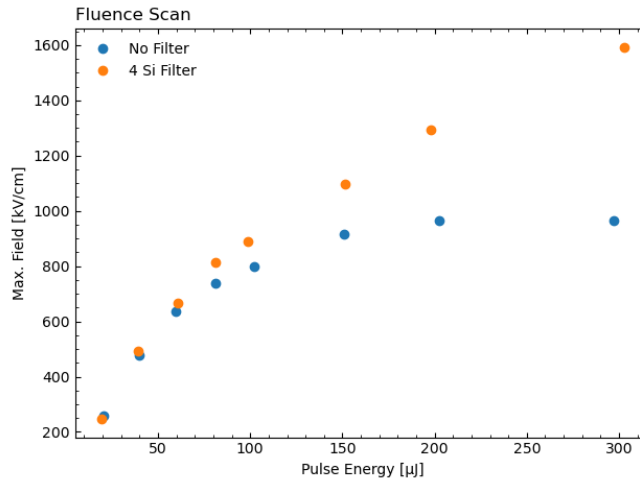
Figure 3.4: Calibration curve
THz field dependent on the pulse energy with additional Si filers (orange) and without (blue). The orange data points have been corrected for the filter-related loss in the low energy regime.

Without additional filters, we can clearly see in Fig. 3.4 that the GaP response saturates and we cannot resolve the actual field strength. However, if we put additional filters just in front of the last parabolic mirror before the GaP (see Fig. 3.2), we allow sample interaction with stronger fields and are still able to measure the field strength properly. For our final measurements, we have chosen six silicon based filters for the better signal to noise ratio obtaining a maximum field of about $1.6 MV/cm$.

3.2 Sample preparation

3.2.1 Construction of cells

The cells; related to the latin word *cella*, which means "small room"; are build to enclose LCs and keep them fixed to a limited volume. This constraint is necessary for the investigation of thermotropic LCs, since the LCs would just flow away if heated up to a strongly liquid-like phase. Furthermore, a

strong alignment of the LCs is required for meaningful analysis of the aniso-tropic vibrational response. The alignment is realised by applying a high AC voltage ($\sim 1kV/1mm$) between two electrodes positioned approximately ($2mm$) apart. As mentioned in section 2.1.1, the electric field determines the molecules orientation $\vec{n}$ and consequently the crystal axes. The electrodes also serve as spacers ($0.5mm$ thick with 5% uncertainty). To prepare our cells, we mainly used cyclo-olefin copolymer (COC) as substrates, which are transparent in the THz range. Measuring the discotic HAT 5 at high temperatures forced us to use *SiC* as window material. Any impurities within the cells would worsen the quality of the experiment and consequently the results. Therefore, an intensive cleaning process; including detergents, Iso-propanol, and Acetone; of the windows and electrodes is indispensable. The length of the process is quite long, thus a rack with space for ten frames allows to speed up this part of the construction. An outline of the process is provided in keywords:

1. Gently rubbing (with gloves) the COC windows in a $250ml$ DI water solution with $2,8mg$ diluted Alconox soap

2. Windows $20min$ in a sonic bath with the detergent solution

3. Windows $3 \times 5min$ in a sonic bath with milli-Q water

4. Windows $15min$ in a sonic bath with Isopropanol

5. Parallel cleaning of the metal wires with Acetone

6. Placing a wire between two windows and clamping it with an alu-minium construction (see Fig. 3.5a)

7. Mixing an epoxy resin with a hardener for glue creation and coating the outer edges (parallel to the electrodes) of the two windows

8. Soldering the electrodes ends in the cell together with the wires that will be later attached to the stage

9. Putting shrinking tubes over the cables and isolating thereby the ends with a heat gun

10. Filling the cell with LC and sealing it with the epoxy based glue (see Fig. 3.5c)

(a)

(b)

liquid crystal

epoxy glue   electrodes

(c)

(d)
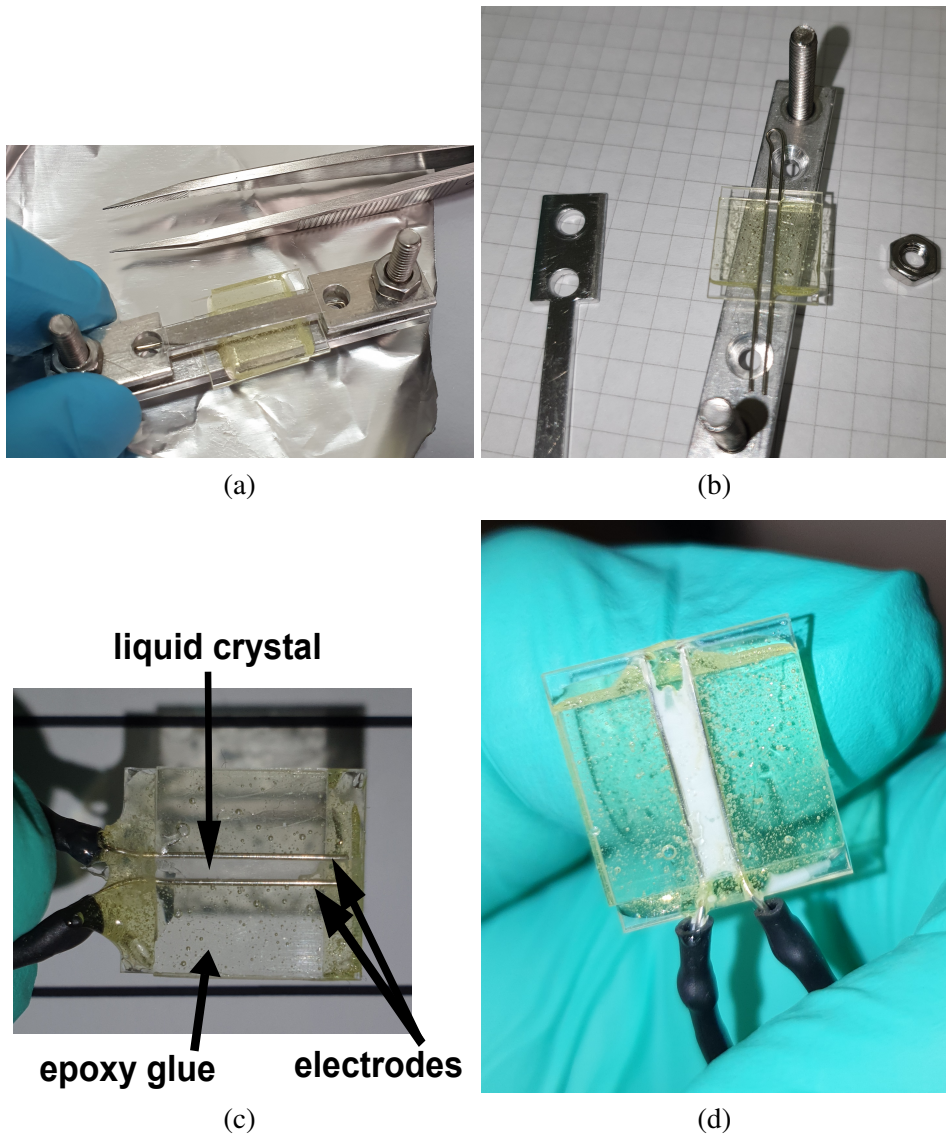
Figure 3.5: Pictures of the cell production.
(a) Placing the windows and a wire, which can later be utilised as electrodes, in a holder that simplifies the gluing of the cells. (b) Cell after the first gluing process. The upper wire loop is cut off before the cell is filled. (c) The cell is filled with the LC and closed with additional epoxy glue. (d) After the cell has been heated up a couple of times, the LC might leak, see (c))

3.2.2   Heating stage

Investigating thermotropic LCs re-
quires a precise control of the LC
temperature. We utilise a heating
stage (Linkam LTS120) for bring-
ing the LC on the desired temperat-
ure and keeping it at a certain tem-
perature during the measurements.
The heating stage is placed perpen-
dicular to the beam path, such that
the beam can propagate through a
hole in its center. However, the tem-
perature assigned to any measure-
ment represents the temperature of
the heating plate and not the actual
temperature of the LC in the cell.
The surrounding air at $20°C$ induces
a temperature gradient within the

Figure 3.6: Cell fixed on the Linkam-Stage

cell. Consequently, the stage temperatures, at which the measurements have
been performed, were chosen such that the behaviour in nematic, smectic
A and isotropic phases can be quantified. This has been validated by ob-
serving the sample at different stage temperatures, under a polarised light
microscope. The temperature stability of the stage is $0.1C$. The electrodes'
contacts, represented by the red, isolated ends, are connected to the high
voltage cable, which is guided through the stage wall (see Fig. 3.6).

Chapter 4

Results and discussions

4.1 8CB in comparison with 8OCB

The two calamitic thermotropic LCs 8CB and 8OCB offer a great possibility to study the influence of the additional oxygen atom in the 8OCB. For obtaining the data in Fig. 4.1, we built cells merely filled with 8CB. We assigned the crystals' ordinary and extraordinary axes (see section 2.1.3) with $n_o < n_e$.
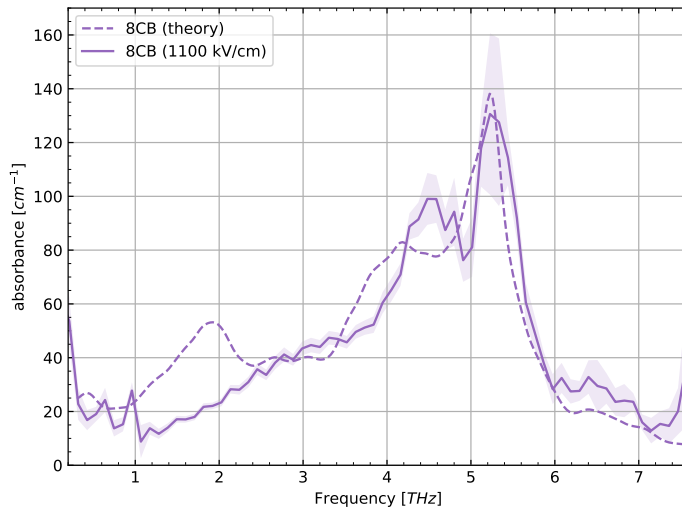
Figure 4.1: 8CB absorbance spectrum in the ordinary axis for the smectic phase at $1100\,kV/cm$. Comparison of theoretically calculated data for the two molecules and the measured absorbance. The theoretical data's frequency scale is rescaled by a factor of 1.019 and the corresponding absorbance is normalised for the 8CB peak at 5.5 THz.

The spectrometer has been validated by comparing measurements of 8CB's ordinary axis for the smectic phase (see Fig. 4.1) with the benchmarked results within the ULCD goup [2]. All spectral features agree very well with [2]. The strong intramolecular band at around $5.5\,THz$ is clearly observable. Likewise, the low-frequency blue-shifting modes' $(1-2.5\,THz)$ of the experimental data relative to the theory, due to intermolecular interaction, is obtained as expected. The discrepancy's cause is the theoretical absorbance that is calculated for single molecules and not for an ensemble of 8CB molecules forming condensed phases [2].

4.1.1   8 OCB analysis

For a more detailed insight in the response of 8OCB, we measured both the ordinary and extraordinary ray for all three phases, see Fig. 4.2. The supplementary data can be found in the Appendix. Note, the theoretically calculated absorbance for 8OCB is also only the mono-molecular response and has been calculated from the same source as in the former work of the research group [2].

(a) ordinary	(b) extraordinary
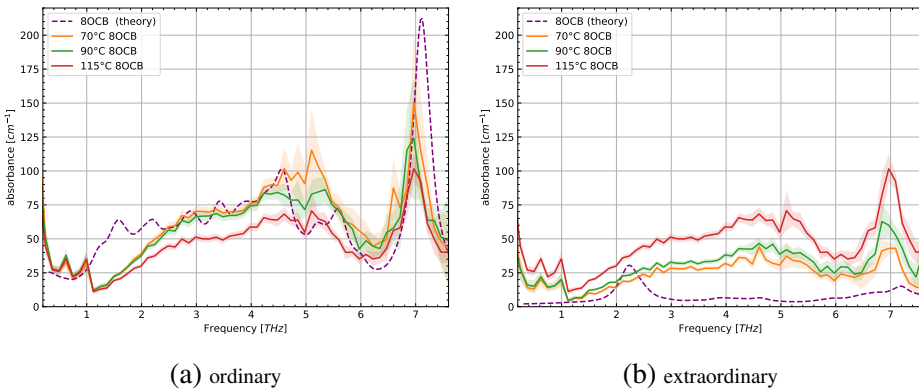
Figure 4.2: Absorbance of 8OCB in (a) the ordinary and (b) extraordinary axes compare the theoretically calculated data with the experiments. The calculation for the extraordinary axis has been done in the same manner as for Fig. 4.1 with the identical rescaling. The temperatures correspond to the following LC phases: $70°C \cong SmA$, $90°C \cong Nm$, and $115°C \cong I$

Having a closer look at 8OCB's ordinary axis (Fig. 4.2a), we observe, similar to 8CB, a discrepancy between theory and experiment in the low-frequency range $(1-2.5\,THz)$, whereas the strongest predicted band at $7\,THz$ is clearly present for all three phases. The low-frequency discrepancy

can underlie intermolecular interactions in a condensed phase and thereby cause a blue-shift in the absorbance, as it is the case for 8CB. However, the assessment of the $7\,THz$ peak's strength is limited due to the dynamic range at this frequency (see Fig. A.4b and Fig. A.4g). The sharp $7\,THz$ band is linked to intramolecular modes. The absorptive response between $2\,THz$ and $5\,THz$ are generally smoothed out, in contrast to the theory. This implies intermolecular interactions in the condensed phase rather than the spectral resolution. However, the spectral resolution is strongly determined by the available time window before the first reflection. The dip at $5\,THz - 5.5\,THz$ is very faint compared to its theoretical prediction and almost non-existent. In addition, the 2nd bigger dip, located around $6.3\,THz$, is also slightly more filled up than expected. We assign also intermolecular interactions for those modulations, since we observe a general smoothing in this regime. Further research is essential to provide a well-founded explanation. Looking at the extra ordinary axis (Fig. 4.2b), we obtain a strong discrepancy between theory and experiment. However, it has to be considered that the alignment of the LCs is not perfect and therefore the molecules with a partial orientation along the ordinary axis contribute to the alleged extraordinary absorbance. The lower the order parameter, the higher the contribution in the extraordinary axis' absorbance. This is clearly evident for the most extreme case, an isotropic state, that has by definition an isotropic refractive index and absorbance. (red curve in Fig. 4.2b) In addition, the cells, more precisely their electrodes, and consequently the LCs are orientated along the incoming polarisation axis by eye which can cause a slight systematic misalignment. The low-frequency modes can also be blue-shifted for the extraordinary axis. Hence, the relatively weak but significant mode around $2.1\,THz$ cannot be resolved.

To deepen our understanding on the spectral feature clearly visible in the experiment, we compare with the theory calculation based on a density functional theory (DFT) method from our collaborator (see Fig. 4.3). The molecule oscillations that are visualised in Fig. 4.3 describe the dipole oscillation dynamics for the according dipole (red arrow). This oscillation is the relaxation of the transient dipole moment driven by the THz field. The $7\,THz$ mode is an oscillation of a dipole, illustrated with a red arrow in Fig. 4.3a, mostly perpendicular to the phenyl rings' planes. We can identify bending of the CN group and the phenyl groups, and torsion at the oxygen atom. The alkyl chain twists (see Fig. 4.3a). A similarly orientated dipole at

$4\,THz$ induces an oscillation of same characteristic motion. In contrast, we could assign oscillation modes for the low-frequency bands $(2\&2.5\,THz)$ to dipoles partially perpendicular and partially parallel to the phenyl ring (see Fig. 4.3d and Fig. 4.3c). The phenyl rings twist relative to each other and cause torsion for both cases. At $2.5\,THz$, the torsion expands along the alkyl chain, whereas the alkyl chain gets stiffer in the case of the $2\,THz$ mode. The DFT calculation revealed also modes that are dipole induced mostly parallel to the phenyl rings' planes, as it is the case for the $5\,THz$ mode (see Fig. 4.3e). The induced motion exhibits identical bending and twisting as the previously described modes at $7\,THz$ and $4\,THz$.

(a) 7 *THz* mode

(b) 4 *THz* mode

(c) 2 *THz* mode

(d) 2.5 *THz* mode

(e) 5 *THz* mode
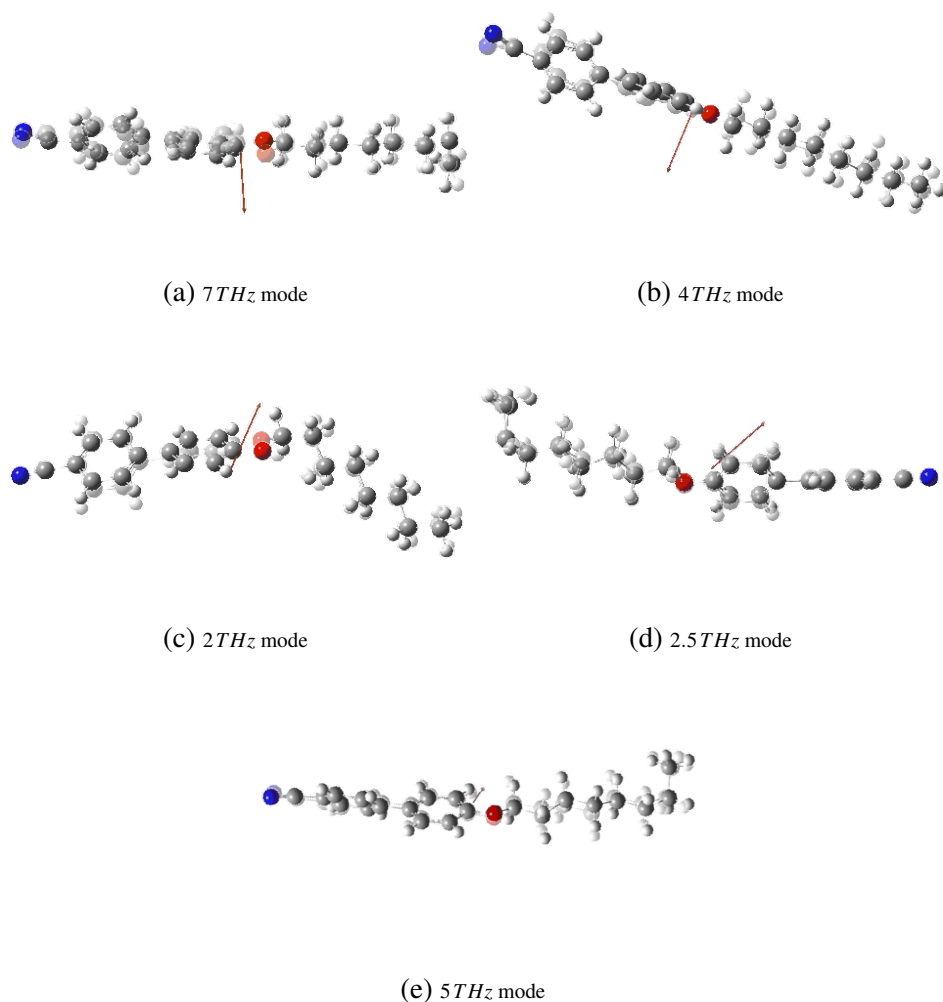
Figure 4.3: Visualisation of the DFT calculations by Dr. Galimberti. The two outermost positions have been chosen for visualising the oscillation motion. One of them is faded, making it recognisable.

Further calculations allowed us to separate the oscillation contribution of the perpendicular dipole components from the parallel dipole components to the phenyl rings' planes. In the following, parallel to the rings' planes means also being perpendicular to the axis determined by the longest molecule dimension. The sum of the perpendicular and parallel component, according to our restrictions, represent the ordinary axes of our LC. In addition, the THz field components correspond to the dipole components, since the dipole

moments responsible for the relaxation oscillations are driven by the THz field. Thus, we can predict the spectral strength of the oscillations for both components separately and compare it with the absorbance in the ordinary axis (see Fig. 4.4). The previously mentioned strong contribution of the perpendicular component to the $7\,THz$ mode and the parallel component (dashed blue) to the $5\,THz$ mode is clearly evident in Fig. 4.4. Moreover, we observe that the perpendicular component (dashed cyan) is responsible for the strong response behaviour at $1 - 2\,THz$ in the theoretical calculation for 8OCB's ordinary absorbance. These low-frequency modes behave differently when the molecules act with each other in a condensed phase. Hence, the blue-shifting of that band explains the experimental data better.
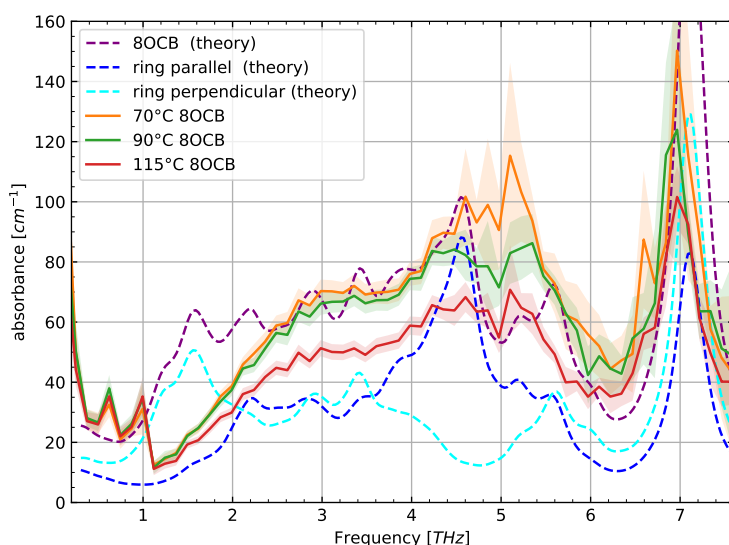
Figure 4.4: Highlighting the contribution of different vibration modes. Vibration-related absorbance driven by field perpendicular (cyan) and parallel (black) to 8OCB's phenyl ring. The curves have been rescaled with the same previous factors as in Fig. 4.2.

4.1.2   Mixtures of 8CB and 8OCB

Given the very similar molecular structure between 8CB and 8OCB, but slightly different chemical composition, we wanted to investigate if the presence of an oxygen atom, characterised by high electronegativity, could establish different dynamics compared to the pure monomolecular LCs. Therefore, we decided studying mixtures of the mass ratios 1 : 1, 3 : 1, and 1 : 3.

    We achieved filling the cells with close to nominal mass ratios by using a precision scale. (For more details see Appendix) The theoretical data plotted in Fig. 4.5 (dashed violet) assumes having neither additional interaction nor specific steric clustering of the molecules, compared to their pure configurations. Consequently, these violet curves are just the linear combination of 8CB's and 8OCB's theoretically calculated absorbances. The curves are labeled with the nominal mass ratios while considering the final ratios. Note that the nematic phase measurement for the 1 : 1 cell has been discarded due to incorrect temperature settings.

    To guide our interpretation, together with the theory curve we represent an experimental curve (dashed blue) which results from the linear summation, considering the ratio of each mixture, of the pure 8CB's and 8OCB's absorbance in the smectic phase. Overall, the mixtures follow both the theory and the 'synthetic' experimental curves.
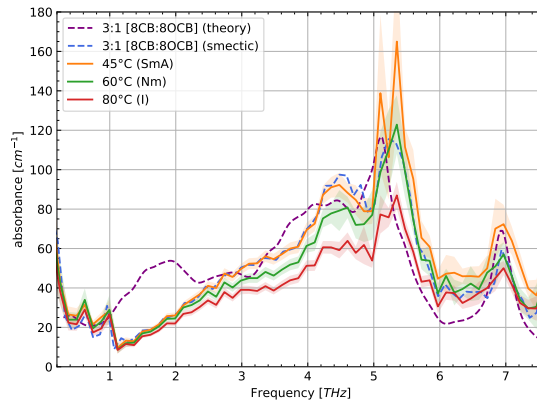
(a) 25% 8OCB, 75% 8CB
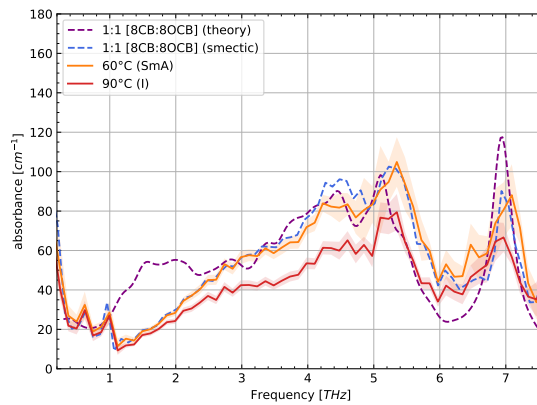
(b) 50% 8OCB, 50% 8CB
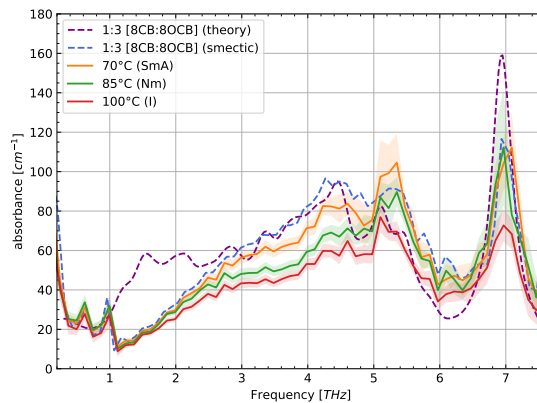
(c) 75% 8OCB, 25% 8CB

Figure 4.5: Absorbance of 8CB / 8OCB mixture cells in the ordinary axis.
The linear combination of 8CB's and 8OCB's individual absorbance spectra are calculated for the theory (violet) and the independently measured data (blue), considering the real mass ratios. The color coding corresponds in the following manner to LC phases: orange $\widehat{=} SmA$, green $\widehat{=} Nm$, and red $\widehat{=} I$.

However, when looking more carefully, the absorption band between $6\,THz$ and $6.5\,THz$ (Fig. 4.1) in pure 8CB is significantly amplified when adding 8OCB (Fig. 4.5a, Fig. 4.5b). This implies not considered interaction between 8CB and 8OCB molecules by the simple summation of the individual spectra. This discrepancy is still present at higher 8OCB concentrations, 75% or 100%, but not of this extent. Consequently, this difference implies that a certain type of intermolecular interaction might not be considered or omitted in pure 8OCB and 8CB and more likely the responsible modes are stronger or of different nature in mixtures with lower 8OCB percentage. In addition, we did the same linear combination for the smectic phase's absorbance (blue graph in Fig. 4.5) with the data from Fig. 4.1 which follows the smectic phase of the mixtures really well. The previously discussed irregularity in the frequency range $6 - 6.5\,THz$ is also present. Moreover, we see a general broadening of the spectrum between $3.5 - 5.5\,THz$ with increasing 8OCB concentration.

4.1.3   Fluence scan of 8CB and 75% 8OCB

We measured the sample's absorbance for different THz field strengths, also known as *fluence scan*, and thereby investigated for non-linear responses of 8CB and 8OCB. The higher field strengths are generated by increasing the pump beam's power and determined as in section 3.1.4. Our five measurements were taken at $600 - 1600\,\mathrm{kV/cm}$ and we had to discard the measurement at the lowest field strength due to irregularities (see Appendix). We were studying a cell filled with 8CB and another cell containing 75% 8OCB and 25% 8CB. Two major trends appear in the absorbance spectrum of the mixed cell (see Fig. 4.6a). The 75% 8OCB cell's absorbance decreases between $4.5 - 5\,THz$ as we intensify the THz field. Whereas, we observe an increasing absorbance between $6\,THz$ and $6.7\,THz$ with increasing THz field strength, broadening our spectrum in that frequency range.

The 8CB fluence scan does not reveal a significant trend, at first glance. Thus, we tried to represent the absorbance with an empirical model of four Lorentz curves (see Fig. 4.7). The first 3 curves did not exhibit a specific trend, whereas we could identify a slight red-shift for the frequency band around $6.5\,THz$. In contrast, applying the previous empirical model on the 75% 8OCB cell data and thereby quantifying dynamics was unfortunately not that successful. (For more details, see Appendix)
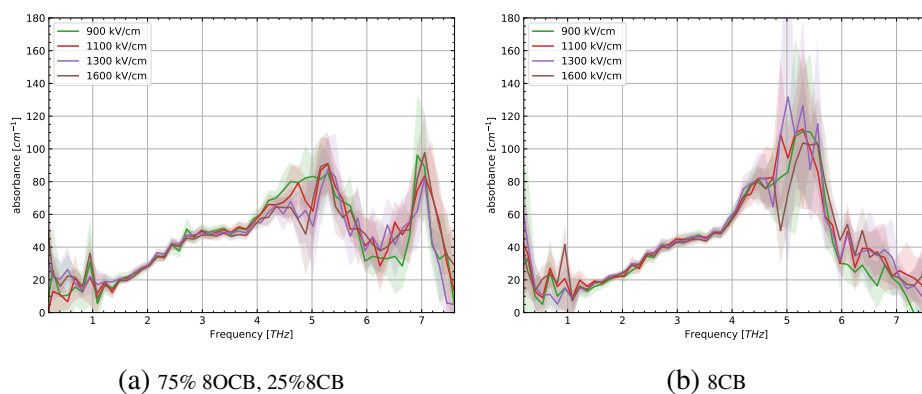
(a) 75% 8OCB, 25%8CB   (b) 8CB

Figure 4.6: Absorbance of a 8CB cell and a 75% 8OCB / 25% 8CB cell at different fluences

Nevertheless, the previously mentioned features in Fig. 4.6a ($4.5 - 5\,THz$ and $6 - 6.7\,THz$) are clearly identifiable without additional analysis. Linking to the discussion of pure 8OCB Fig. 4.1, the frequency band between $6\,THz$ and $6.5\,THz$, which also has been mentioned to be higher than expected for pure 8OCB, is even higher in the mixed cell the more intense the THz field is. This implies non-linear interaction between the two different molecules in the mixed cell.

(a) 900kV/cm

(b) 1100kV/cm

(c) 1300kV/cm

(d) 1600kV/cm

(e) fitted curves (individual)

(f) fit parameters
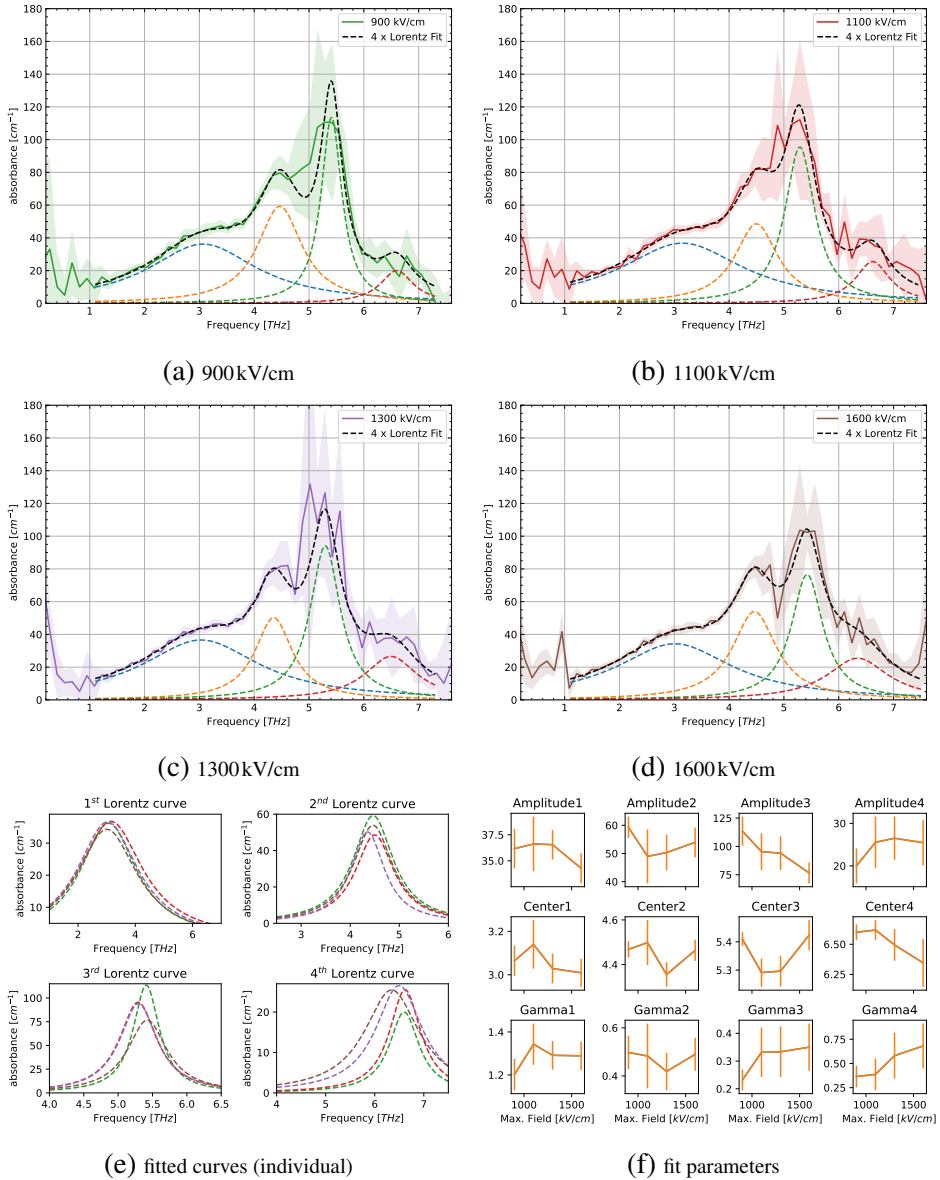
Figure 4.7: Fitting the absorbance of 8CB for different fluences with empirical model (a-b) and (d-e) show the fit in the spectra. The dashed lines represent the fit results. (c) presents the fit results of each individual Lorentz curve for all four fluences, color coded as in Fig. 4.6. (f) visualises the variation the 3 fitting parameter for all four fluences, including uncertainties.

4.2 Discotic LCs

Compared to the calamitic LCs that we have used, the clearing temperature of HAT5 and HAT4 are significantly higher. Hence, we had to use cell windows that were not melting, which was why we chose 4H-SiC. Unfortunately, it is not possible to align the LCs' molecules by an external electric field, since there are no significant permanent dipoles within the molecules. Instead, we cooled down the LCs from the isotropic to the columnar phase at a very low rate $(0.03°C/\text{min})$, since this possibly allows natural alignment. We received an almost perfect homeotropic alignment for the HAT4 (see Fig. A.15). However, the HAT5 sample was in a polydomain state (see Fig. A.13) during the measurements, which could influence the obtained spectra of our data. The influence would be that we do not probe the ordinary or extraordinary axes, but an unknown combination of them and consequently could not draw meaningful conclusions. Nevertheless, the isotropic phase allows rigorous interpretation, since it is the average of all orientations. Regarding both HAT4 and HAT5, we could clearly see that the isotropic phase is absorbing stronger than the columnar phase over the entire range from $1 - 6\,THz$ (see Fig. 4.8). Having a closer look at the dynamic range reveals that the absorbance above $6.5\,THz$ is slightly limited in its amplitude (see Fig. A.14d & Fig. A.12d).

In the homeotropic columnar phase, the extraordinary axis is parallel to the substrate normal. Thus, we solely measure the ordinary axes of the crystals. The difference between the isotropic and columnar phase implies a significantly stronger absorbance in the extraordinary axis than the ordinary axes. We can see a slight red-shift for some modes around $4\,THz$ of HAT4, when comparing the spectrum with HAT5. At least, the absorbance of HAT5 is more broadened. A possible explanation could be a higher stiffness or rigidity, the longer the alkoxy groups.
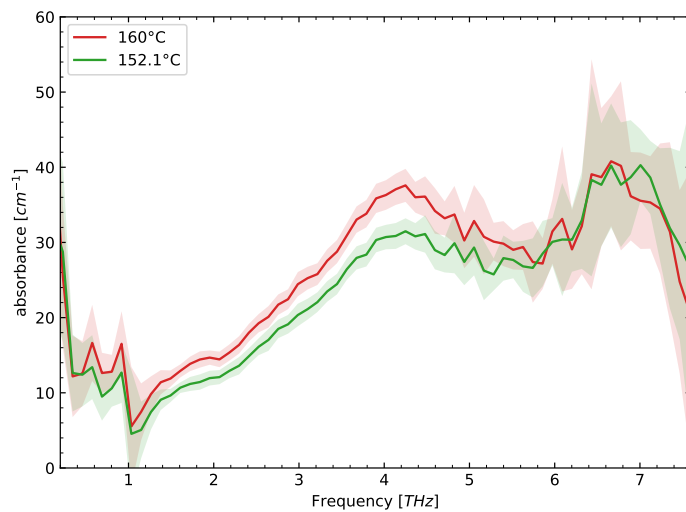
(a) HAT4
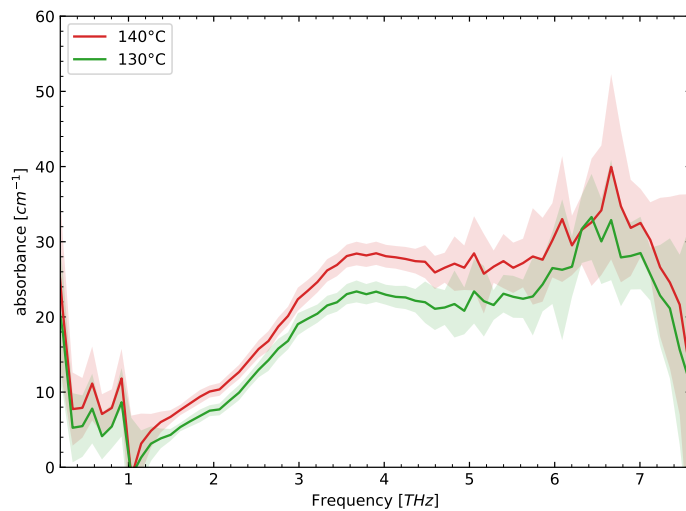
(b) HAT5

Figure 4.8: Absorbance of HAT4 and HAT5. The cells contained a sample volume with the thickness of $700\mu m$. We have measured the isotropic phases (red) and colunar phases (green).

Chapter 5

Conclusions

The studies of 8OCB revealed interesting discrepancy with the theory. Regarding the absorbance, we could assign blue-shifting in the low-frequency range $(1 - 2.5\,THz)$, we observed a general smoothing out of the spectrum (especially wihtin $1.5 - 4.5\,THz$), and measured an unclear difference at $5\,THz$ in the ordinary axis. Quantifying the strength of the characteristic peak at $7\,THz$ has to be realised in a future experiment with a thinner cell and consequently a larger dynamic range. This absorbance band must be linked to the additional oxygen atom, enabling new modes in the molecule. Moreover, 8CB's fluence scan showed minimal non-linear activity, in our range of field modulation, except potential red-shifting of high frequency modes around $6.5\,THz$. In contrast, the cell that was filled with 75% 8OCB exhibited a clear non-linear response. The absorbance strongly decreases at $5\,THz$ and the dip between $6 - 6.5\,THz$ is less deep the higher the THz's field strength. We assign the latter together with the potential modulation of 8CB in this regime to a common non-linear response of both LCs. Nevertheless, finding the causes of this behaviour demands theoretically calculated absorbance that encounters field strength dependent interaction. The DFT calculations for pure 8CB and 8OCB just consider molecule oscillations and not the driving force dependency, which corresponds to the field strength. This nominal frequency range is also pointing out as we mixed 8CB and 8OCB in different mixtures at constant pump beam power. At lower 8OCB concentration, the discrepancy between the theoretical predicted absorbance and the experimental data was even stronger than at high 8OCB concentration. Consequently, the intermolecular interaction between 8CB and 8OCB

is strong in this regime and amplified at higher field strengths, when considering the fluence scans.

Our measurements of HAT4 and HAT5 showed that we were able to align discotic LCs even in thick cells. The absorbance spectra revealed significantly stronger absorbance in the extraordinary axis than in the ordinary axis for both HAT4 and HAT5. Comparing HAT4 with HAT5 indicates higher stiffness of the HATn molecules, the longer the alkoxy groups get.

Bibliography

[1] F. Reinitzer. *Beiträge zur Kenntniss des Cholesterins*. Monatshefte für Chemie - Chemical Monthly, 1888.

[2] Patrick Friebel, Daria Ruth Galimberti, Matteo Savoini, and Laura Cattaneo. Unveiling low thz dynamics of liquid crystals: Identification of intermolecular interaction among intramolecular modes. 2023. doi:10.1021/acs.jpcb.3c07947.

[3] Paul van der Schoot. *Molecular Theory of Nematic (and Other) Liquid Crystals*. Springer Cham, 2022. doi:10.1007/978-3-030-99862-2.

[4] Wenbo Shen and Guoqiang Li. Recent progress in liquid crystal-based smart windows: Materials, structures, and design. *Laser & Photonics Reviews*, 17(1), 2023. doi:10.1002/lpor.202200207.

[5] Sadiara Fall, Jing Wang, Thomas Regrettier, Nicolas Brouckaert, Olzhas A. Ibraikulov, Nicolas Leclerc, Yaochen Lin, Mohammed Ibn Elhaj, Lachezar Komitov, Patrick Lévêque, Yuhan Zhong, Martin Brinkmann, Malgosia Kaczmarek, and Thomas Heiser. Self-powered dynamic glazing based on nematic liquid crystals and organic photovoltaic layers for smart window applications. *ACS Applied Materials & Interfaces*, 15(3):4267–4274, 01 2023. doi:10.1021/acsami.2c21727.

[6] Satyendra Kumar. *Liquid Crystals: Experimental Study of Physical Properties and Phase Transitions*. Cambridge University Press, 2001.

[7] Cyrus R et al. Safinya. Liquid crystal assemblies in biologically inspired systems. *Liquid crystals*, 40:1748–1758, 2013. doi:10.1080/02678292.2013.846422.

[8] P.G. de Gennes and J.Prost. *The Physics of Liquid Crystals*. Oxford University Press, 1993.

[9] Denis Andrienko. Introduction to liquid crystals. *Journal of Molecular Liquids*, 267:520–541, 2018. ISSN 0167-7322. doi:10.1016/j.molliq.2018.01.175. Special Issue Dedicated to the Memory of Professor Y. Reznikov.

[10] Leonaş Dumitraşcu, Irina Dumitraşcu, and Dana-Ortansa Dorohoi. External Electrostatic Field Influence on the Order Parameter of Nematic Liquid Crystalline Thin Layers. *AIP Conference Proceedings*, 899(1): 317–318, 04 2007. ISSN 0094-243X. doi:10.1063/1.2733164.

[11] Kiranmala Thingujam, Ayon Bhattacharjee, Basana Choudhury, and Roman Dabrowski. Nematic liquid crystals exhibiting high birefringence. *Optical Review*, 23(3):409–419, 2016. doi:10.1007/s10043-016-0207-9.

[12] Abir Aouini, Maurizio Nobili, Edouard Chauveau, Philippe Dieudonné-George, Gauthier Damême, Daniel Stoenescu, Ivan Dozov, and Christophe Blanc. *Chemical-Physical Characterization of a Binary Mixture of a Twist Bend Nematic Liquid Crystal with a Smectogen*. crystals, 2020. doi:10.3390/cryst10121110.

[13] Subhadip Ghosh and Arun Roy. Crystal polymorphism of 8ocb liquid crystal consisting of strongly polar rod-like molecules. *RSC Adv.*, 11: 4958–4965, 2021. doi:10.1039/D0RA08543J.

[14] Şükrü Özgan and Mustafa Okumuş. Thermal and spectrophotometric analysis of liquid crystal 8cb/8ocb mixtures. *Brazilian Journal of Physics*, 41(2):118–122, 2011. doi:10.1007/s13538-011-0034-1.

[15] A. Zidanšek, G. Lahajnar, and S. Kralj. Phase transitions in 8cb liquid crystal confined to a controlled-pore glass: Deuteron nmr and small angle x-ray scattering studies. *Applied Magnetic Resonance*, 27(1): 311–319, 2004. doi:10.1007/BF03166325.

[16] G.A. Oweimreen and M.A. Morsy. Dsc studies on p-(n-alkyl)-p'-cyanobiphenyl (rcb's) and p-(n-alkoxy)-p'-cyanobiphenyl (rocb's) liquid crystals. *Thermochimica Acta*, 346(1):37–47, 2000. ISSN 0040-6031. doi:10.1016/S0040-6031(99)00411-6.

[17] Piero Morales, Jan Lagerwall, Paolo Vacca, Sabine Laschat, and Giusy Scalia. Self-assembled ordered structures in thin films of hat5 discotic liquid crystal. *Beilstein Journal of Organic Chemistry*, 6:51, 2010. ISSN 1860-5397. doi:10.3762/bjoc.6.51. URL https://doi.org/10.3762/bjoc.6.51.

[18] Asmita Shah, Dharmendra Pratap Singh, Benoit Duponchel, Freddy Krasisnski, Abdelylah Daoudi, Sandeep Kumar, and Redouane Douali. Molecular ordering dependent charge transport in π-stacked triphenylene based discotic liquid crystals and its correlation with dielectric properties. *Journal of Molecular Liquids*, 342:117353, 2021. ISSN 0167-7322. doi:https://doi.org/10.1016/j.molliq.2021.117353. URL https://www.sciencedirect.com/science/article/pii/S0167732221020778.

[19] Qiao Zheng, Guojia Fang, Weibin Bai, Nanhai Sun, Pingli Qin, Xi Fan, Fei Cheng, Longyan Yuan, and Xingzhong Zhao. Efficiency improvement in organic solar cells by inserting a discotic liquid crystal. *Solar Energy Materials and Solar Cells*, 95(8):2200–2205, 2011. ISSN 0927-0248. doi:https://doi.org/10.1016/j.solmat.2011.03.024. URL https://www.sciencedirect.com/science/article/pii/S0927024811001772. Photovoltaics, Solar Energy Materials & Thin Films, IMRC 2009-Cancun.

[20] Qijun Liang, Shanpeng Wang, Xutang Tao, and Thomas Dekorsy. Temperature dependence of free carriers and lattice vibrations in novel nonlinear optical crystals in the thz frequency regime. pages 1–1, 2017. doi:10.1109/CLEOE-EQEC.2017.8086439.

[21] Xinwei Li, Dasom Kim, Yincheng Liu, and Junichiro Kono. *Terahertz spin dynamics in rare-earth orthoferrites*. 2022. doi:10.48550/arXiv.2209.09468.

[22] Keita Yamaguchi, Takayuki Kurihara, Hiroshi Watanabe, Makoto Nakajima, and Tohru Suemoto. Dynamics of photoinduced change of magnetoanisotropy parameter in orthoferrites probed with terahertz excited coherent spin precession. *Phys. Rev. B*, 92:064404, Aug 2015. doi:10.1103/PhysRevB.92.064404.

[23] Hassan A. Hafez, Sergey Kovalev, Klaas-Jan Tielrooij, Mischa Bonn, Michael Gensch, and Dmitry Turchinovich. Terahertz nonlinear optics of graphene: From saturable absorption to high-harmonics generation. *Advanced Optical Materials*, 8(3):1900771. doi:10.1002/adom.201900771.

[24] Chia-Jung Yang, Jingwen Li, Manfred Fiebig, and Shovon Pal. Terahertz control of many-body dynamics in quantum materials. *Nature Reviews Materials*, 8(8):518–532, 2023. doi:10.1038/s41578-023-00566-w.

[25] D. Oepts, A.F.G. van der Meer, and P.W. van Amersfoort. The free-electron-laser user facility felix. *Infrared Physics & Technology*, 36(1): 297–308, 1995. ISSN 1350-4495. doi:10.1016/1350-4495(94)00074-U.

[26] Fabio Novelli, Biswajit Guchhait, and Martina Havenith. *Towards Intense THz Spectroscopy on Water: Characterization of Optical Rectification by GaP, OH1, and DSTMS at OPA Wavelengths*. materials, 2020. doi:10.3390/ma13061311.

[27] R. Paschotta. *Nonlinear Polarization*. RP Photonics AG, Feb 2005. doi:10.61835/iuv.

[28] Bahaa E. A. Saleh and Malvin Carl Teich. *Fundamentals of Photonics*. John Wiley & Sons, 2013. doi:10.1002/0471213748.

[29] Yun-Shik Lee. *Principles of Terahertz Science and Technology*. Springer, 2009. doi:10.1007/978-0-387-09540-0.

[30] Robert W. Boyd. *Nonlinear Optics*. Academic Press, 2020. doi:10.1016/C2015-0-05510-1.

[31] C. Vicario, M. Jazbinsek, A. V. Ovchinnikov, O. V. Chefonov, S. I. Ashitkov, M. B. Agranat, and C. P. Hauri. High efficiency thz generation in dstms, dast and oh1 pumped by cr:forsterite laser. *Opt. Express*, 23(4):4573–4580, Feb 2015. doi:10.1364/OE.23.004573.

[32] P.U. Jepsen, D.G. Cooke, and M. Koch. Terahertz spectroscopy and imaging – modern techniques and applications. *Laser & Photonics Reviews*, 5(1):124–166. doi:10.1002/lpor.201000011.

[33] Bernd Richard Steffen. Electro-optic methods for longitudinal bunch diagnostics at flash. 2007. doi:10.3204/DESY-THESIS-2007-020.

[34] Marco P. Fischer, Johannes Bühler, Gabriel Fitzky, Takayuki Kurihara, Stefan Eggert, Alfred Leitenstorfer, and Daniele Brida. Coherent field transients below 15thz from phase-matched difference frequency generation in 4h-sic. *Opt. Lett.*, 42(14):2687–2690, Jul 2017. doi:10.1364/OL.42.002687.

[35] Jens Neu and Charles A. Schmuttenmaer. Tutorial: An introduction to terahertz time domain spectroscopy (THz-TDS). *Journal of Applied Physics*, 124(23):231101, 12 2018. ISSN 0021-8979. doi:10.1063/1.5047659.

[36] Peter Uhd Jepsen. Phase retrieval in terahertz time-domain measurements: a "how to"tutorial. *Journal of Infrared, Millimeter, and Terahertz Waves*, 40(4):395–411, 2019. doi:10.1007/s10762-019-00578-0.

[37] R. Paschotta. *Thermal Radiation*. RP Photonics AG, Apr 2019. doi:10.61835/dhr.

Appendix A

I. diagrams

A.1 Planck's law (THz generation)

The spectral radiance of a blackbody for frequency v at absolute temperature T is given by [37]:

$$L_{v,\Omega}(v,T) = \frac{2hv^3}{c^2} \frac{1}{\exp\left(\frac{hv}{k_B T}\right) - 1}. \tag{A.1}$$

For presenting an upper limit of the irradiance, we look at the radiance over the whole solid angle

$$L_v(v,T) = \frac{8\pi hv^3}{c^2} \frac{1}{\exp\left(\frac{hv}{k_B T}\right) - 1}, \tag{A.2}$$

and integrate over the THz range for different Temperatures.

The integral between $0.1\,THz$ and $10\,THz$ at $T = 300K$ represents a power of $< 203W/m^2$.
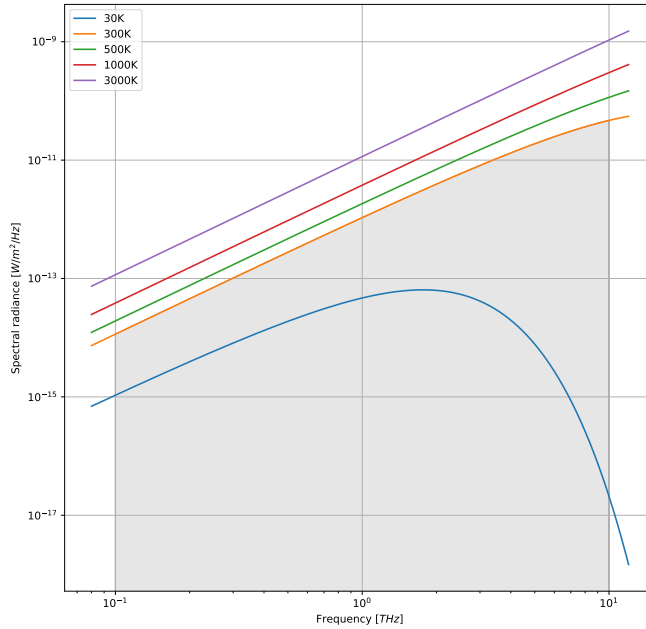
Figure A.1: Spectral irradiance of blackbodies at different absolute temperature T
The shaded area represents the exemplar integral for $T = 300K$.

A.2   Elliptical polarisation

First, we study the propagation of the probe beam assuming it to be of cw
nature. The linearly polarised probe beam's electric field, before entering
the GaP crystal, can be expressed in the principle axes A and B,

$$E_A = \frac{E_0}{\sqrt{2}} \sin \omega t \,, \tag{A.3}$$

$$E_B = \frac{E_0}{\sqrt{2}} \sin \omega t \,, \tag{A.4}$$

where E_0 is the amplitude of the incoming signal, and we have chosen
the phase appropriately. Note, that we will choose the phase for the later
cases such that the relative phase between A and B is clear and intuitive.
Subtantialy, we will study an exemplar time, e.g. $t = t_0$, considering the

non-trivial case, $E_{THz} \neq 0$, in the GaP. Without loss of generality, we can assume $n_A > n_B \iff v_A < v_B$ and calculate the transmission coefficients according to Eq. (2.33),

$$t_1^A \cdot t_2^A = \frac{2}{1+n_A} \frac{2n_A}{n_A+1} = \frac{4n_A^2}{(n_A+1)^2}, \tag{A.5}$$

$$t_1^B \cdot t_2^B = \frac{2}{1+n_B} \frac{2n_B}{n_B+1} = \frac{4n_B^2}{(n_B+1)^2}, \tag{A.6}$$

The transition coefficients describe the intensity remainder and consequently the square root of it describes the electric field remainder. The phase shift Eq. (2.24) has to be added to E_A, since the A-axis is the slower axis. The electric field E' that passed the GaP crystal is described by:

$$E_A' = \frac{E_0}{\sqrt{2}} \frac{2\sqrt{n_A}}{n_A+1} \sin\left(\omega t + \Delta\phi\right), \tag{A.7}$$

$$E_B' = \frac{E_0}{\sqrt{2}} \frac{2\sqrt{n_B}}{n_B+1} \sin\left(\omega t\right), \tag{A.8}$$

and if we assume the $\lambda/4$-plate fast axis to be the A-axis, we obtain the electric field E'' before entering the detector,

$$E_A'' = \frac{E_0}{\sqrt{2}} \frac{2\sqrt{n_A}}{n_A+1} \cos\left(\omega t + \Delta\phi\right), \tag{A.9}$$

$$E_B'' = \frac{E_0}{\sqrt{2}} \frac{2\sqrt{n_B}}{n_B+1} \sin\left(\omega t\right), \tag{A.10}$$

A.3   Data Set 8CB
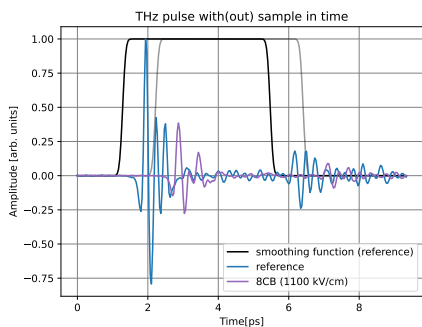
(a) TD (ordinary)
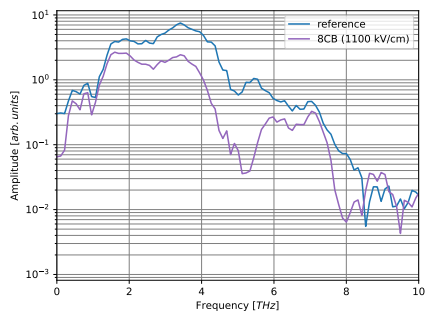
(b) FD (ordinary)
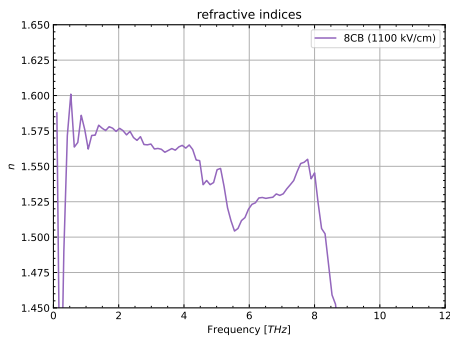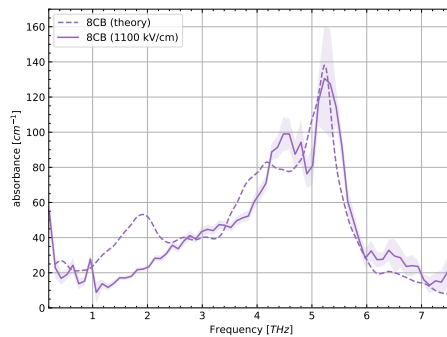
(c) n (ordinary)

(d) absorbance (ordinary)

Figure A.2: Full data set of the 8CB measurement at 1100 kV/cm

A.4   Irregular reference in the fluence scan

If we compare all the five references, we can clearly see that the $20\,mW$ reference exceeds the noise level significantly. Fig. A.3 We increased the signal amplification ($\times 10$) during all experiments at this power due to weak signal strength. This may have caused this issue and therefore we won't consider this data.
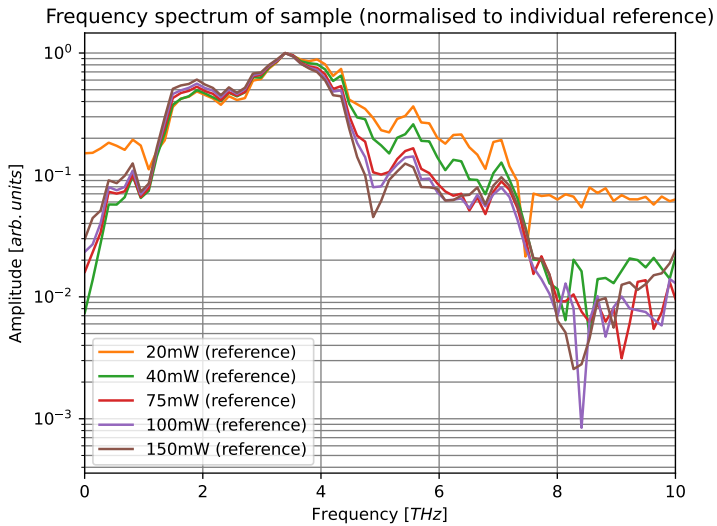
Figure A.3: Normalised reference spectra, with respect to the individual maximum, for the different fluences.

A.5   8 OCB anaylsis

(a) TD (ordinary)

(b) FD (ordinary)

(c) n (ordinary)

(d) TD (extraordinary)

(e) FD (extraordinary)

(f) n (extraordinary)

(g) Dynamic range for the absorbance (ordinary) with a reasonable noise floor, $\approx 5 \cdot 10^{-3}$ a.u., in the FD spectrum
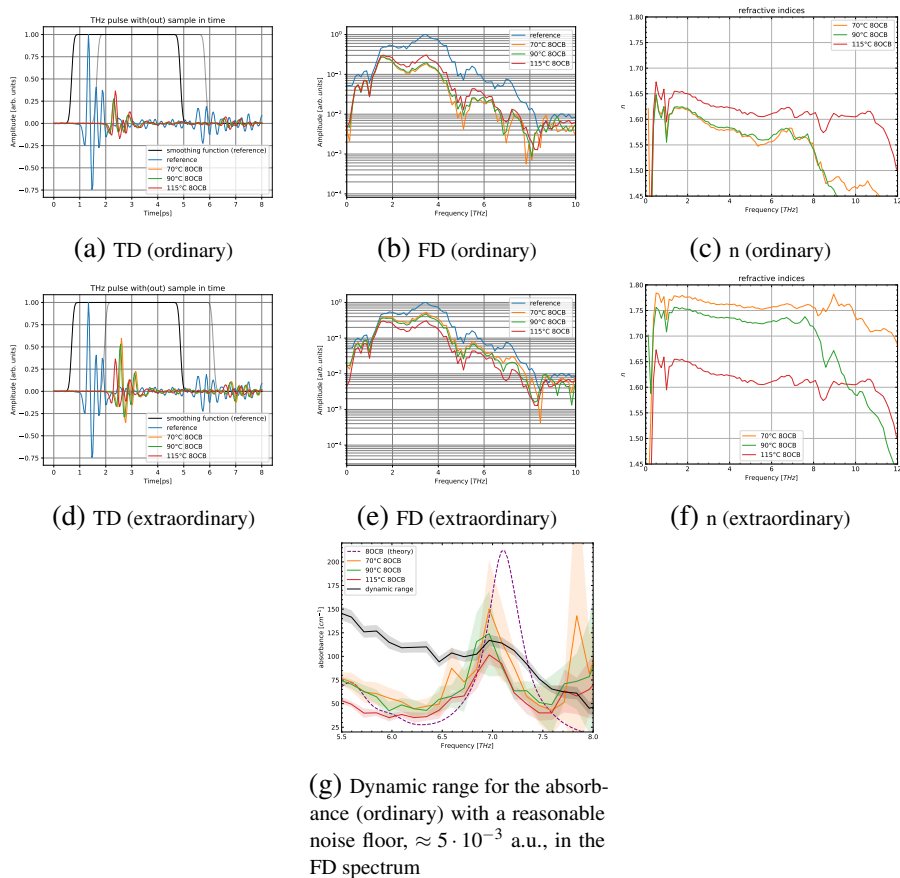
Figure A.4: The additional plots to the data acquisition of the entire 8 OCB scan (ordinary and extraordinary axes). The ordinary axis corresponds to the fast axis, having a lower refractive index than the extraordinary axis.

A.6 Mixtures of 8CB and 8OCB

A.6.1 Mass ratios

We let off the previous volumetric filling approach and swapped to a mass based filling. Thereby, we improved our technique and changed from plastic pipettes to thicker glass pipettes which don't cool down so fast and thus enabled transporting a 8OCB portion in a liquid-like phase. The referred mass ratios, given by integers, represent the ratios which were intended to reach while building the cells. The actual mass ratios differ slightly and are estimated in the last column of Table A.1. The expected absorbances for the mixtures' nematic phase, Fig. 4.5, are the summation; encountering the final mass ratio; of the experimentally measured nematic absorbance for pure 8CB and 8OCB.

Expected mass ratio [8CB:8OCB]	m_{8OCB} [mg]	m_{8CB} [mg]	Final mass ratio
$3:1$	31.32	12.27	$\approx 2.56:1$
$1:1$	19.27	21.27	$\approx 0.91:1$
$1:3$	21.80	59.87	$\approx 1:2.75$

Table A.1: Mass ratios of the mixtures that were used to fill the cells.

A.6.2   Full data set

(a) TD (25% 8OCB)   (b) TD (50% 8OCB)   (c) TD (75% 8OCB)

(d) FD (25% 8OCB)   (e) FD (50% 8OCB)   (f) FD (75% 8OCB)

(g) n (25% 8OCB)   (h) n (50% 8OCB)   (i) n (75% 8OCB)

(j) absorbance (25% 8OCB)   (k) absorbance (50% 8OCB)   (l) absorbance (75% 8OCB)
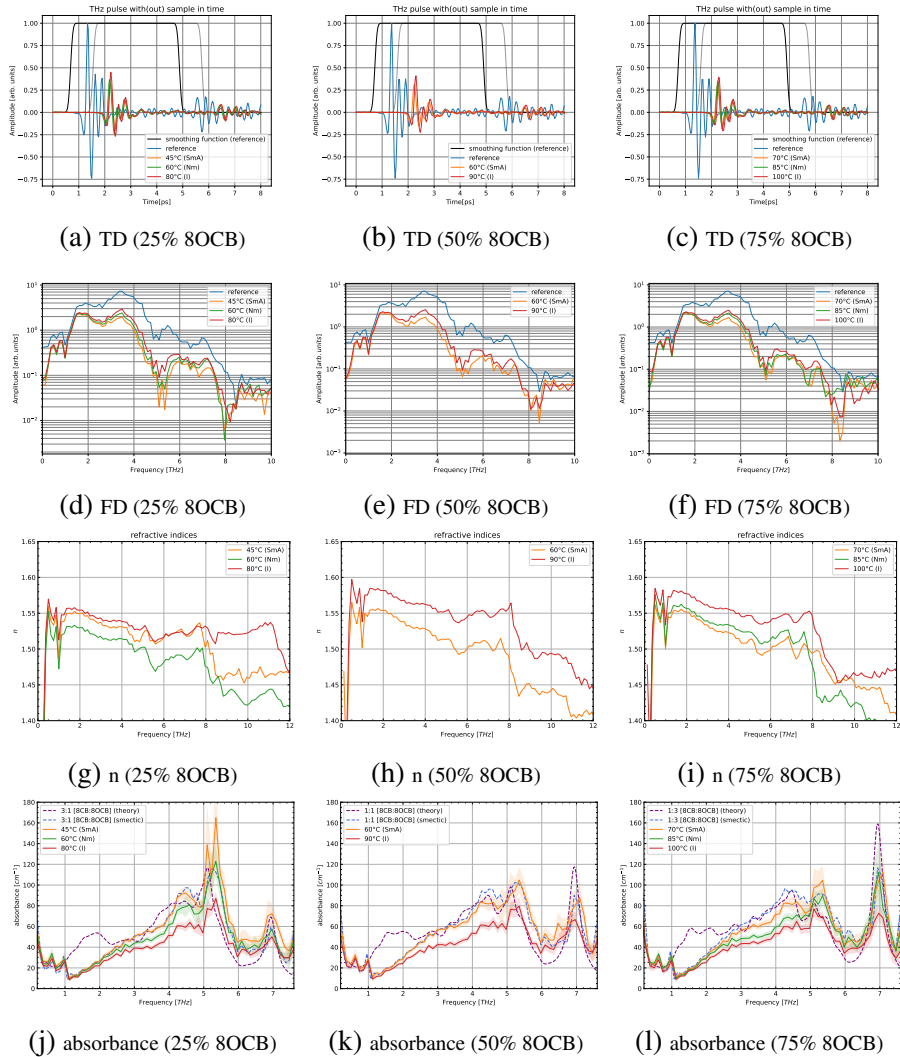
Figure A.5: Full data set for all three 8CB/8OCB mixtures in the ordinary axis. (j-l) already include the theoretically calculated curves that are mentioned in section 4.1.2.
1st row: TD pulses , 2nd row: FD spectra, 3rd row: refractive indices, 4th row: absorbance.

A.7　8CB fluence scan

A.7.1　Full data set
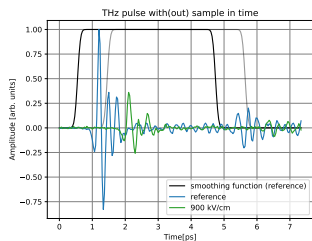
(a) TD (900 kV/cm)
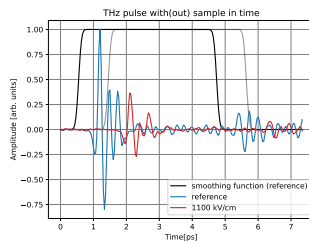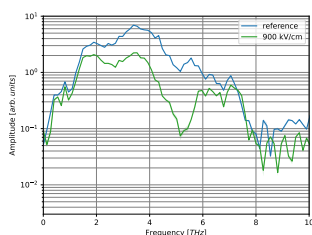
(b) TD (1100 kV/cm)

(c) FD (900 kV/cm)
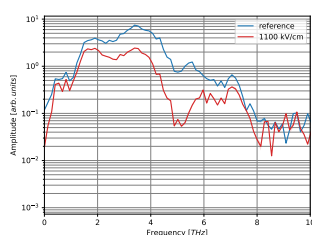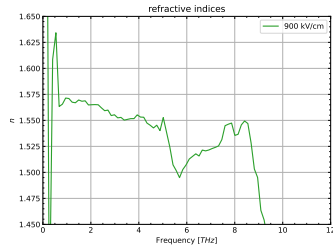
(d) FD (1100 kV/cm)
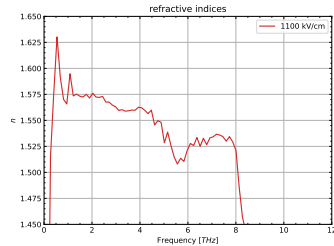
(e) n (900 kV/cm)
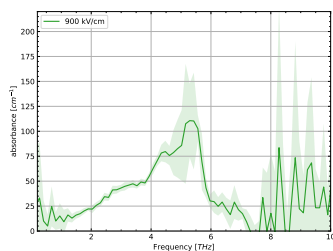
(f) n (1100 kV/cm)

(g) absorbance (900 kV/cm)
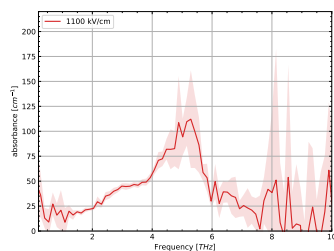
(h) absorbance (1100 kV/cm)

Figure A.6: Full data set of 900kV/cm and 1100kV/cm measured for the 75% 8OCB cell. 1st row: TD pulses , 2nd row: FD spectra, 3rd row: refrective indices, 4th row: absorbance
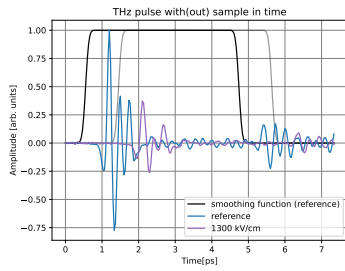
(a) TD (1300 kV/cm)
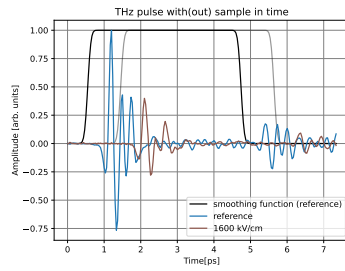
(b) TD (1600 kV/cm)
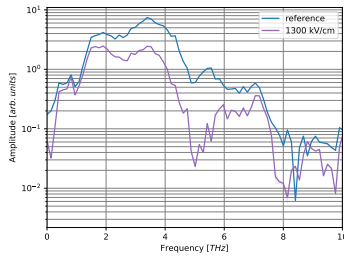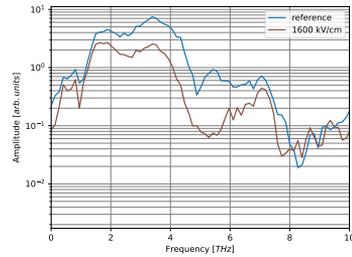
(c) FD (1300 kV/cm)
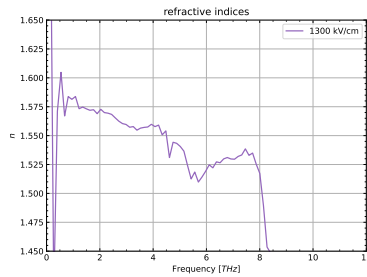
(d) FD (1600 kV/cm)
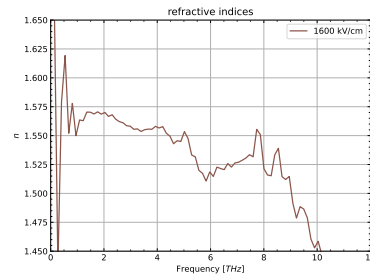
(e) n (1300 kV/cm)
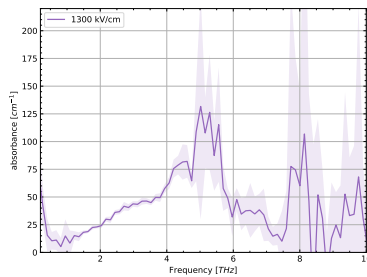
(f) n (1600 kV/cm)

(g) absorbance (1300 kV/cm)
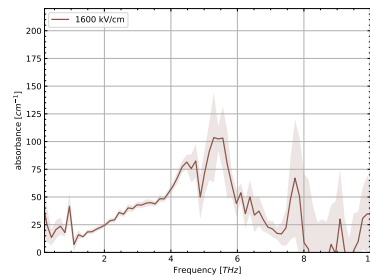
(h) absorbance (1600 kV/cm)

Figure A.7: Full data set of 1300kV/cm and 1600kV/cm measured for the 8CB cell.
1st row: TD pulses , 2nd row: FD spectra, 3rd row: refractive indices, 4th row: absorbance

A.7.2 Fitting the 8CB spectra

We have chosen to model the absorbance of 8CB with 4 Lorentz curves. This is an empirical model that seems to fit the data quite well (see Fig. 4.7). The only significant trend is observed for the highest frequency modes. (4th Lorentz curve) We register a slight red-shift and an increase in amplitude as the field strength increases. The authenticity may be questioned.

(a) (b)
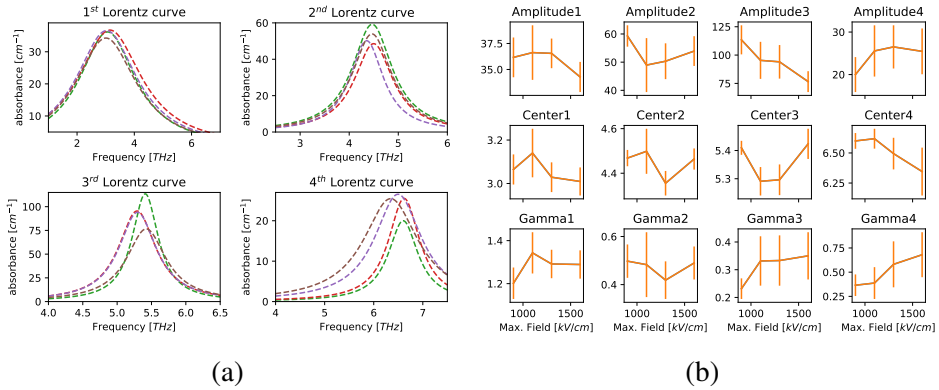
Figure A.8:
(a) Fitted Lorentz curves curves for the five different fluences (same color code as in Fig. 4.6b).
(b) Fitting parameter corresponding to 4 Lorentz curves describing the absorbance between $1.1\,THz$ and $7.5\,THz$.

A.8　75% 8OCB fluence scan

A.8.1　Full data set
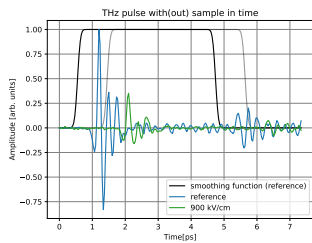
(a) TD (900 kV/cm)
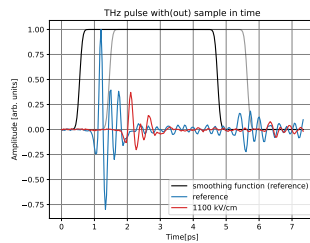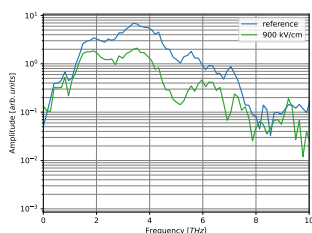
(b) TD (1100 kV/cm)

(c) FD (900 kV/cm)
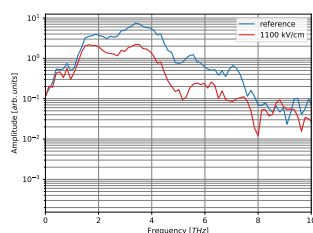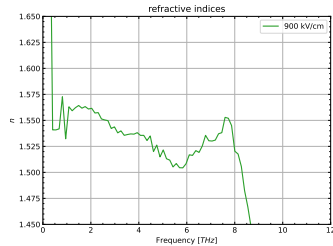
(d) FD (1100 kV/cm)
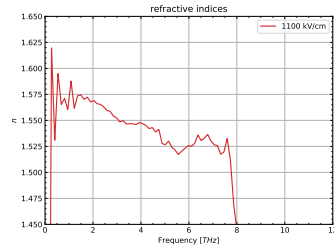
(e) n (900 kV/cm)
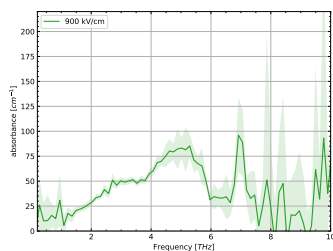
(f) n (1100 kV/cm)

(g) absorbance (900 kV/cm)
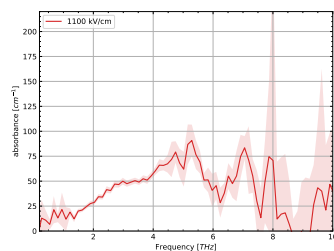
(h) absorbance (1100 kV/cm)

Figure A.9: Full data set of 900kV/cm and 1100kV/cm measured for the 75% 8OCB cell.
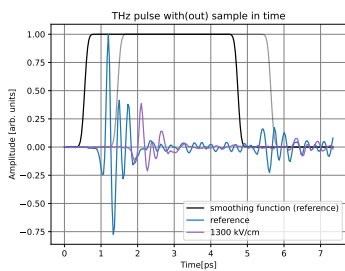
(a) TD (1300 kV/cm)
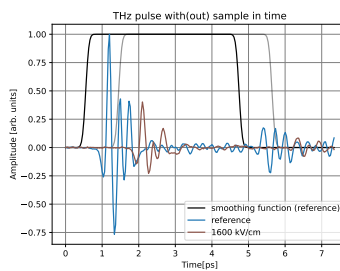
(b) TD (1600 kV/cm)
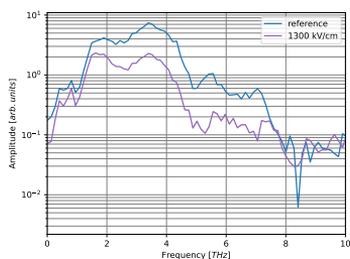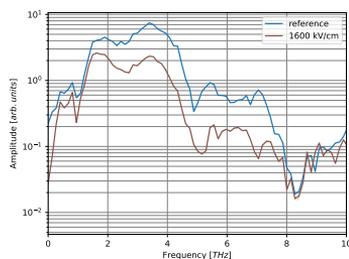
(c) FD (1300 kV/cm)
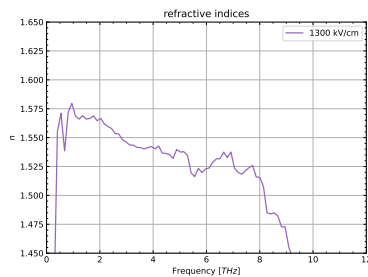
(d) FD (1600 kV/cm)
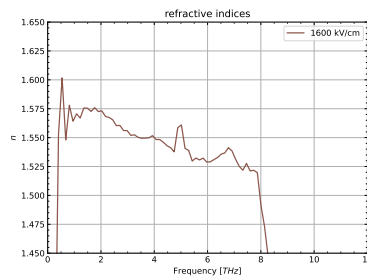
(e) n (1300 kV/cm)
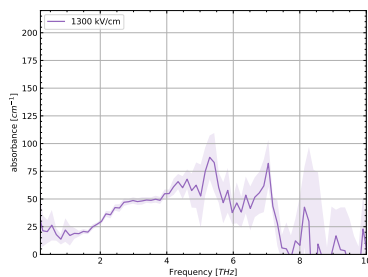
(f) n (1600 kV/cm)

(g) absorbance (1300 kV/cm)
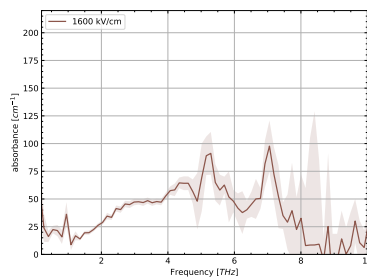
(h) absorbance (1600 kV/cm)

Figure A.10: Full data set of 1300kV/cm and 1600kV/cm measured for the 75% 8OCB cell.

A.8.2   Fitting the 75% 8OCB spectra

(a) 900 kV/cm

(b) 1100 kV/cm

(c) 1300 kV/cm

(d) 1600 kV/cm

(e) individual comparisson
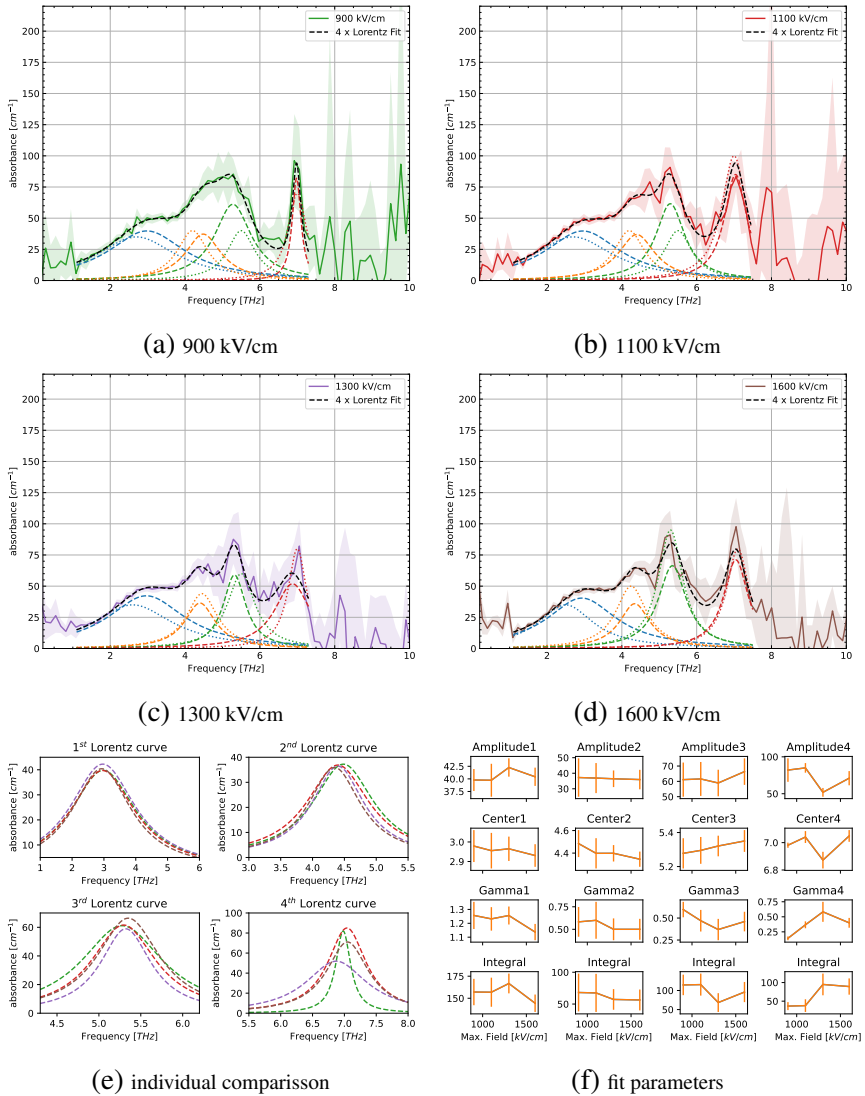
(f) fit parameters

Figure A.11: Fitting the absorbance spectra of all fluences measured for the 75% 8OCB cell. The fit parameters can be seen in (f).

A.9   HAT5 - complete data set

(a) TD

(b) FD

(c) n

(d) Dynamic range with a noise floor of $\approx 2 \cdot 10^{-3}$ a.u.
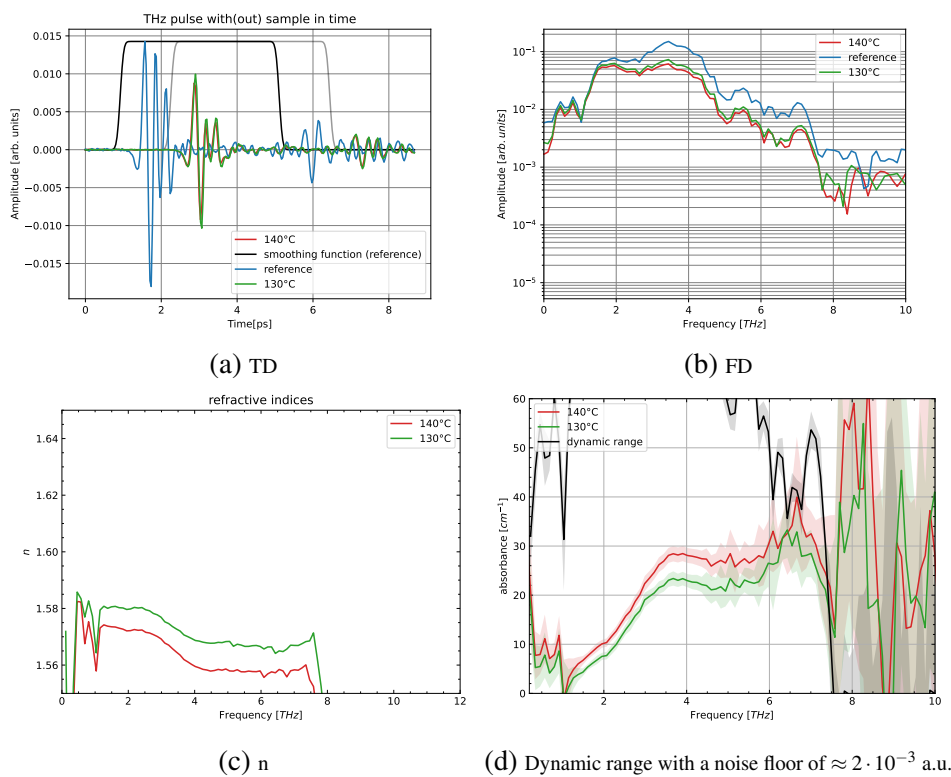
Figure A.12: Full data set of HAT5 measured in the crystalline phase at $30°C$ (orange), the columnar phase at $130°C$ (green) and the isotropic phase at $140°C$ (red).
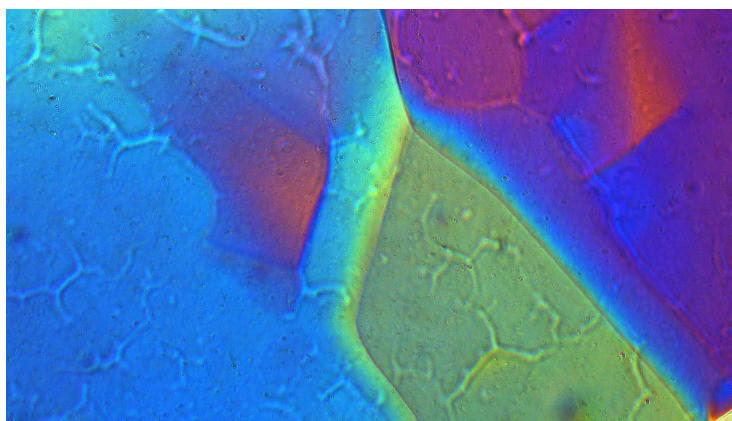
Figure A.13: Columnar phase (HAT5) at $130°C$ under a polarised light microscope. A polydomain is clearly identifiable.

A.10   HAT4- complete data set

(a) TD

(b) FD

(c) n

(d) Dynamic range with a noise floor of $\approx 2 \cdot 10^{-3}$ a.u.
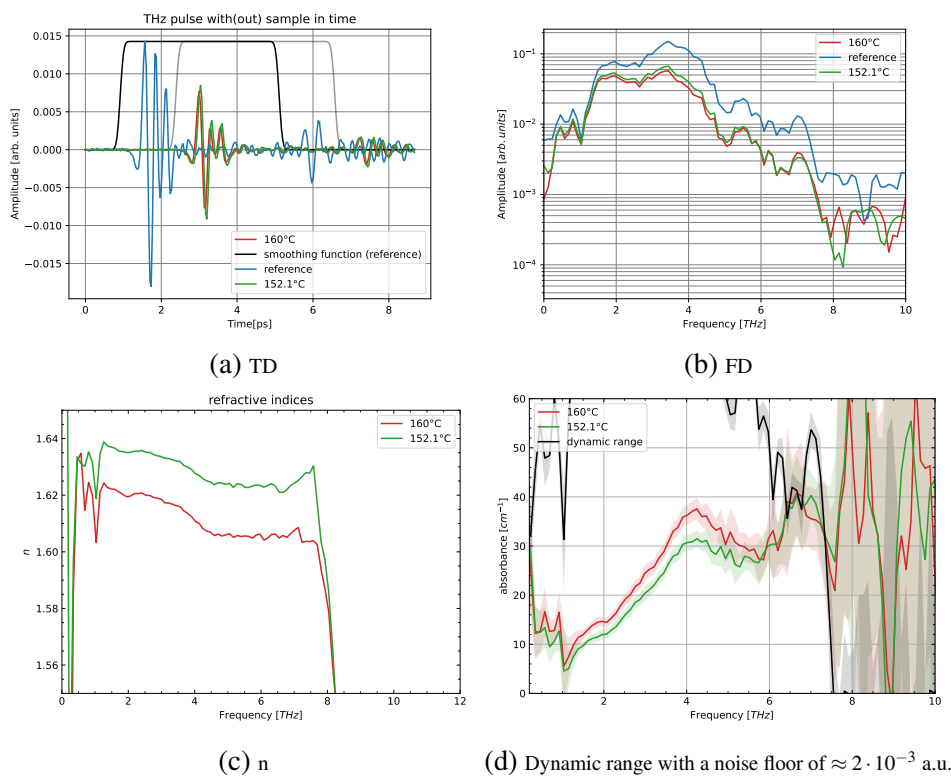
Figure A.14: Full data set of HAT4 measured in the crystalline phase at $50°C$ (orange), the columnar phase at $152.1°C$ (green) and the isotropic phase at $160°C$ (red).
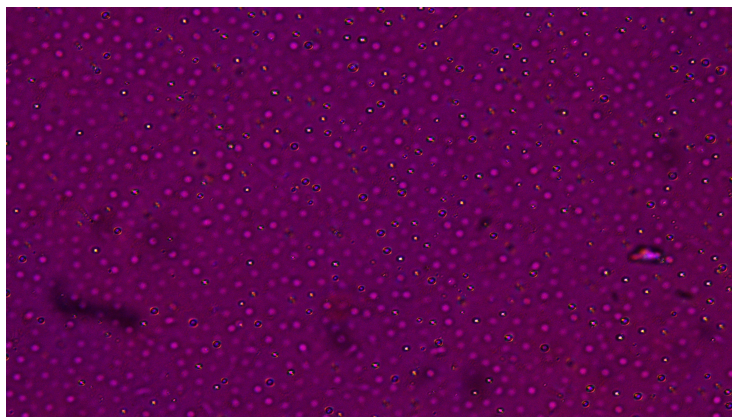
Figure A.15: Columnar phase (HAT4) at $152.1°C$ under a polarised light microscope.